A LONG BASELINE OPTICAL INTERFEROMETER FOR ASTROMETRY

By

MICHAEL SHAO

S.B. M.I.T. 1971

SUBMITTED IN PARTIAL FULFILLMEMT OF

THE REQUIREMENTS FOR THE DEGREE OF

DOCTOR OF PHILOSOPHY

at the

MASSASSCHUSETTS INSTITUTE OF TECHNOLOGY

September, 1978

Signature of Author Signature redacted
Department of Physics

Certified by Signature redacted
Thesis Supervisor

Accepted by Signature redacted

A LONG BASELINE OPTICAL INTERFEROMETER FOR ASTROMETRY

By

MICHAEL SHAO

Submitted to the Department of Physics in August 1978, in partial fulfillment of the requirements for the degree of Doctor of Philosophy.

Abstract

A new type of astrometric instrument, the astrometric interferometer, is described. The instrument is a long baseline Michelson stellar interferometer modified to track the fringe motion caused by atmospheric turbulence. Simultaneous fringe amplitude and phase measurements at two wavelengths are used to correct atmospheric distortion when the field of view is much larger than the isoplanatic patch. Ultimately, the relative positions of stars brighter than 10 mag in a one degree field of view could be measured to 0.0001 to 0.00001 arc sec accuracy in a single observation lasting several hours. Such an instrument should have a number of interesting astrophysical and geophysical applications, such as a search for planets around nearby stars, the gravitational deflection of light, and changes in the earth's rotation axis. This thesis describes the first steps in the development of an astrometric interferometer.

Thesis Supervisor: David H. Staelin
Professor of Electrical Engineering and Computer Science

Acknowledgements

These first steps towards the development of an astrometric interferometer would have not been possible without assistance from a number of sources. I would like to thank Prof. B. Burke for the loan of the PDP 8 computer, and Prof. D. Troxel for the use of his computer facilities for software development. I am also grateful for the donated machine shop time from Prof. H. Bridge and to D. C. Papa who designed most of the mechanical components of the prototype. I would also like to acknowledge the support of the faculty at Wellesly College Observatory and Prof. T. McCord at Wallace Observatory during the initial tests of the prototype interferometer. Most of all, I would like to thank Prof. D. Staelin whose support and encouragement from the very beginning made this thesis possible.

Table of Contents

I Introduction

Astrometry, the precise measurement of stellar positions, is one of the oldest and historically important branches of astronomy. When Galileo invented the telescope in the early 1600's astronomy changed radically. Observations of planetary motion led Copernicus to a heliocentric theory of the solar system, and accurate measurements of the position of the planet Mars by T. Brahe led Kepler to formulate his three laws. Accurate visual measurements with telescopes led to the discovery of the planet Neptune while verifying both Newton's law of gravity and the mathematical perturbation techniques that were used to predict its existance and location. Accurate astrometry also led to the discovery of the aberration of starlight in 1728 by Bradley, and the finite velocity of light in 1675 by Romer.

With the invention of photography, the accuracy of astrometric measurements was again radically improved. By 1904, Schlesinger at Yerkes Observatory had analysed the errors inherent in photography and had devised measurement procedures and data reduction techniques to minimize these errors. These procedures have often been called basic and complete with only minor improvements possible. It might be added that Schlesinger after leaving Yerkes, set up astrometric programs at half a dozen observatories, and many of them continue to employ Scheslinger's techniques today.

The early photographic measurements of parallax by Hertzsprung led to the Hertzsprung Russel diagram which is the basis for theories of stellar evolution. In addition, astrometry has confirmed the gravitational deflection of light, measured the precession of the perihelion of Mercury, and possibly discovered the presence of planets around Barnard's star.

After Scheslinger's methods were adopted, astrometry flourished. The reduction of major sources of error for photographic astrometry made it possible to achieve 0.01 arc sec accuracy by averaging several years of data. Futher improvement in accuray would require even more time and consequently the field lost its glamour and was viewed as one which required a great deal of tedious work. The current trend is to amass decades of data with which it is hoped, even higher accuracies could be achieved. In the early 60's a comparison of parallax measurements at different observatories [1] showed that systematic errors and not random errors were limiting the accuracy of measurements.

The history of stellar interferometry began with Fizeau [2] who suggested in 1868 the use of an interferometer to measure stellar diameters. In 1921 Michelson and Pease [3] pulbished the first measurement of a stellar diameter. The instrument was the famous 20 foot interferometer which was attached to the 100 inch telescope on Mount Wilson. The next major interferometer was a 50 foot baseline instrument built

by Pease during the years 1923 and 1930. The 50 foot baseline interferometer was plagued by a number of problems. Kababian[4] pointed out an effect due to polarization which reduced the fringe visibility of stars not on the celestial equator. In addition, the 50 foot interferoemter unlike the 20 foot interferometer used an east-west baseline rather than a north-south baseline and was much more sensitive to errors in the sidereal drive.

In the late 60's the advances in photomultipliers and electronics revived interest in spatial interferometers [5]. When Labeyrie demonstrated speckle interferometry in the early 70's [6] interferometers were once again considered new exciting astronomical instruments with great potential. One of these potentials was the ability to make extremely accurate astrometric measurements. Both theory and observational evidence published before 1975 showed that techniques such as speckle and the traditional Michelson interferometer could only achieve high accuracy in a very small field of view, perhaps only a few arc sec.

This thesis is an experimental and theoretical study of an astrometric interferometer. It started when I realized that a two color technique, described in chapter 3 [7] could correct the errors caused by the atmosphere when the field of view was much larger than the isoplanatic patch. A prototype interferometer with a one inch aperture was built and was used to make atmospheric measurements at Wallace observatory (MIT).

The analysis of the measurements showed that proper operation of the interferometer would not be possible at Wallace. The reason was that short integration time neccessary to freeze the atmosphere was much shorter at Wallace Observatory (1-2 msec) than at a good site (10 msec). A method to determine the optimum integration time using 'seeing' measurements was developed. In addition a method for measuring the absolute parallax of a star without the use of reference stars was developed.

Chapter two describes the optical effects of atmospheric turbulence. A brief history of early reasearch in this area is given. While atmospheric turbulence is not considered a major source of error in photographic astrometry, turbulence is the main problem for new high spatial resolution and high accuracy photoelectric astrometric instruments. Chapter two presents the experimental and theoretical work in optical propagation through turbulence that is relevant to astronomy, in order to provide a background for the next few chapters.

Current astrometric techniques are reviewed in chapter three. The first section describes the instruments used to measure relative position of stars. Recently built astrometric instruments such as SCLERA are discussed. The limitating performance, due to atmospheric turbulence, of current astrometric instruments is derived. The application of current instruments to the measurement of proper motion and parallax are discussed in the second section.

The principle of the astrometric interferometer is described in chapter four. Although the accuracy of the instrument is unaffected by the atmosphere, the interferometer, like all high spatial resolution that must look through turbulence, will not work if the star is dimmer than a certain threshold. The limiting magnitude and the accuracy are calculated for an interferometer located at a good astronomical site. The two color technique which enables the interferometer to correct the errors that would limit the performance of conventional astrometric instruments is discussed.

Chapter five discribes the hardware and software of the one inch aperture prototype built for Wallace Observatory. The three major subsystems, laser interferometer, star tracker, and fringe tracker are described as are possible future improvements, especially to the fringe tracking servo.

The atmospheric measurements at Wallace Observatory are described in chaper six. All high resolution instruments use short exposures or integration times to freeze the atmosphere. Currently, astronomical observations with speckle and other interferometers determine the optimum integration time by a trial and error method. A method for estimating the optimum integration time or detector bandwidth from angle of arrival fluctuation data is discussed.

Chapter seven describes several possible applications of an astrometric interferometer with 10^{-4} to 10^{-5} arc sec

(chap 4) accuracy. These applications include the measurement of parallax and the search for planets. The sensitivity of several techniques for the search for planets are also compared.

II Atmospheric Turbulence

While astronomers have known about scintillation and seeing for hundreds of years, and Maxwell's equations were formulated in the 1870's, no systematic study of seeing was done until the 1950's. The first theoretical study of the optical effects of turbulence was by Chandrashakar [8] in 1952. Most of the work preceeding this was qualitative in nature[9]. Since then, and especially recently, a great deal of progress, experimental and theoretical, has been made.

As an electromagnetic wave propagates through the atmosphere, the wavefront is distorted by inhomogeneities in the index of refraction of the atmosphere. The random nature of the distortion requires that the mathematical discription of the optical effects of atmospheric turbulence be statistical. A method of analysis involving structure functions, spatial and temporal correlation functions, is currently used in the study of atmospheric seeing and scintillation.

Seeing and scintillation are caused by spatial and temporal fluctuations in the refractive index of the atmosphere. The index of refraction fluctuations are in turn caused by temperature differences since pressure fluctuations are quickly damped out. In theory, humidity fluctuations would also cause index of refraction fluctuations. In practice this is not important for optical propagation in clear weather. The change in the index of

refraction per unit change in humidity is aproximately 70 times less at optical wavelengths than at radio wavelegths [10]. Unlike temperature variations, humidity variations must originate from a large body of water. For an astronomical observatory at high altitude many miles from a large body of water, and in clear weather, it should be safe to assume that index of refraction variations are due primarily to temperature variations.

The temperature fluctuations originate from large scale heating of the earth's surface. Wind flow and turbulence mixes cold and warm air to create temperature fluctuations of many scale sizes. The index of refraction of the atmosphere n is a function of space and time as expressed in eq. II.1.

$$n(r) = n_0 + n_1(r) \qquad \text{(II.1)}$$

The autocorrelation of the variable part of the index of refraction can then be written as eq. II.2 and its fourier transform eq. II.3.

$$B_n(r) = \langle n_1(\vec{r}_1)\, n_2(\vec{r}_2) \rangle \qquad \text{II.2}$$

$$r = |\vec{r}_1 - \vec{r}_2|$$

$$\Phi(K) = \frac{1}{2\pi K} \int B_{n_1}(r)\, r \sin(Kr)\, dr \qquad \text{II.3}$$

where K is spatial frequency

As wind shear breakes up temperature inhomogeneities to smaller and smaller sizes, the inner scale of turbulence will be reached where the viscosity of the air will prevent further turbulent

mixing. Index of refraction fluctuations are therefore expected to exist with scale sizes between the outer scale, the scale at which temperature fluctuations are created by heating, and the inner scale determined by the viscosity of the air. Work on turbulence by Kolmogorov, Obukhov, and others [11,12] led Tatarski [13] to use eq. II.4 for the refractive index power spectrum.

$$\Phi(K) = 0.033\, C_n^2\, K^{-11/3}\, e^{-K^2/K_m^2} \qquad \text{II.4}$$

$K_m = 5.9/l_o$

l_o is the inner scale of turbulence

The equation is not expected to be valid for spatial frequencies lower than the corresponding frequency for the outer scale. This model of the atmosphere has two parameters, the inner scale l_o(Km) and the refractive index structure constant C_n^2, which is a measure of the strength of turbulence. From dimensional analysis, C_n^2 has the units meters$^{-2/3}$. Obviously, if another model of the atmosphere with another power law were used, the constant would have different units. Measurements of C_n^2 show that this parameter varies from 10^{-18} at high altitudes to 10^{-13} at sea level[14].

Attempts to measure depolarization effects for optical propagation have yielded null results[15]. As a result, all theoretical calculations treat the electric field as a scalar quantity. For atmospheric propagation the wave equation would be eq. II.5.

$$[\nabla^2 + k^2 n^2(r)]\, E = 0 \qquad \text{II.5}$$

k = wave number $2\pi/\lambda$

Tatarski and most others during the 1960's used the Rytov method which substitutes $\Psi = \ln(E)$ into II.5 to get II.6. The real part of Ψ is the log amplitude χ and the imaginary part is the phase ϕ. The procedure was to solve II.6 for fluctuations in with a perturbation technique.

$$\nabla^2\psi + \nabla\psi \cdot \nabla\psi + k^2 n^2 = 0 \qquad \text{II.6}$$

The Rytov method is accurate only when the perturbations are small. Recent theoretical calculations have used the extended Huygens-Fresnel principle. The starting point is a Green's function representation of the electric field. The electric field at the receiver or telescope is related to the electric field at the star by eq. II.7.

$$E(L,r) = \iint d^2r_1\, E_0(r_1) \times \exp\left[i k/2L\, (r-r_1)^2 + \psi(r,r_1) - ikL \right] \qquad \text{II.7}$$

where E_0 is the field at the star

L is the distance to the star

k is the wave number $2\pi/\lambda$

Ψ is the complex phase caused by the turbulence

In order to evaluate statistical quantities involving E at the receiver, it is necessary to evaluate the statistics of the Green's function. The calculations[16] are quite lengthy and complicated and will not be attempted here. The results of the

calculations relevant to astronomy will be discussed in the following sections.

II.A Scintillation

The simplest way to test a theory of turbulence is the measurement of scintillation. For ground to ground experiments, the temperature spatial correlation function can be measured and C_n^2 calculated. Direct verification of the theory is then possible. However, usually only a small number of temperature sensors are used and it is often necessary to assume that the turbulence is homogeneous throughout the optical path.

II.A.1 Intensity distribution

Most theoretical calculations predict that turbulence will produce a log normal distribution for intensity or amplitude. In Rytov's method, the solution to eq. II.6 for $\psi - \langle\psi\rangle$ would be an integral equation. Applying the central limit theorem to the integral would result in a normal distribution for the log amplitude. A normal distribution in the log amplitude implies a normal distribution in the log intensity. If however, the substitution of $\psi = \ln(E)$ were not made, the same procedure would result in a normal distribution in the amplitude. For small variances the difference between the two distributions would be small. However significant differences exist for moderate and

large variances.

The physical interpretations of the two distributions are very different. A normal distribution in E-<E> would mean that the electric field would consist of a constant part and a component with a normal distribution. In the limit where the constant part was small, the intensity distribution would be an exponential or Raleigh distribution. A physical arguement which would favor the log normal distribution goes as follows. The turbulence in the optical path can be viewed as a large number of thin layers of air. Each layer acts as a lens with random properties. The effect is that each layer affects the intensity of light in a multiplicative fashion. When the central limit theorem is applied, valid because of the large number of layers, the distribution in intensity would be a log normal distribution. For a normal distribution in the electric field, each layer would have to affect the electric field in an additive rather than a multiplicative manner. A possible model for the additive effect is that the atmosphere contains a large number of scattering centers. For optical propagation in clear weather the log normal distribution is probably more accurate.

The Rytov method, which is valid for small perturbations, gives eq. II.8 [9] for the variance in the log intensity.

$$\sigma_{lnI}^2 = 2.24\, k^{7/6} \int_0^L C_n^2(z)\,(L-z)^{5/6}\, dz \qquad \text{II.8}$$

k is the wave number

L is the length of the optical path through air

turbulence is assumed locally isotropic

Numerous experiments [18,19] have verified the log normal distribution. Equation II.8 has been verified for weak turbulence [20] where $\sigma_{lnI} < 2.5$. Scintillation measurements at 0.63 and 10.6 microns have also verified the wavelength dependence of II.8 [21]. For strong turbulence, the measured variance σ_{lnI}^2 saturates at a value between 2 and 3 [22]. The saturation effect is not predicted by II.8. Fortunately, for astronomical observations, scintillation is almost never in the saturation region.

II.A.2 Spatial Correlation of Scintillation

The correlation of intensity fluctuations at different points in space may be calculated using the Rytov method. The correlation function of the log amplitude is defined by eq. II.9.

$$B_\chi(r) = \langle \chi(\vec{r}_1)\,\chi(\vec{r}_2) \rangle \qquad \text{II.9}$$

where $r = |\vec{r}_1 - \vec{r}_2|$ and $\vec{r}_i$ is the position at which the log amplitude is measured

For the astronomically relevant case, $B_\chi(r)$ is given by eq. II.10 [9].

$$B_\chi(r) = 4\pi^2\, 0.033\, k^2 \int_0^L dz\, C_n^2(z) \times \int_0^\infty dK\, K\, J_0(Kr)\, K^{-11/3} \exp(-K^2/K_m^2) \sin^2\left(\frac{L-z}{2k}\right) K^2 \qquad \text{II.10}$$

k is the wave number

K is the spatial frequency

r is the distance between measured points

L the length of the optical path through air

J_0 is the Bessel function

In order to compare theory with experiment, it is necessary to relate the log amplitude spatial correlation to the intensity spatial correlation. Following reference [9], the normalized correlation of intensity can be defined as eq. II.11, and reduced to eq. II.12.

$$b_I(r) = \frac{\langle I(r_1)\, I(r_2)\rangle - \langle I(r_1)\rangle\langle I(r_2)\rangle}{\left[\langle I^2(r_1)\rangle\langle I(r_2)\rangle\right]^{\frac{1}{2}} - \langle I(r_1)\rangle\langle I(r_2)\rangle} \qquad \text{II.11}$$

$$b_I(r) = \frac{B_\chi(r)}{\sigma_\chi^2} \qquad \text{II.12}$$

$$\text{where } \sigma_\chi^2 = \frac{1}{4}\,\sigma_{\ln I}^2$$

The importance of II.10 is that it predicts that scintillations will be essentially uncorrelated for two points separated by a distance greater than $(\lambda L)^{1/2}$, where L is typically 10 kilometers for astronomical observations. The scintillation correlation distance is typically 7-8 cm. For a stellar interferometer with a baseline of several meters, the uncorrelated scintillation will result in a fringe visibility below unity. The resulting loss in the signal to noise ratio is discussed in greater detail in chapter 4.

Observations of the spatial correlation of scintillation have essentially verified eq. II.10 for weak scintillation[23]. Photographs of the "shadow bands" from starlight [24] have shown the width of the bands to be 7-8 cm.

From the spatial correlation function it is possible to derive two related quantities. The first is the temporal spectrum of scintillation and the second is the dependence of the log intensity variance on the size of the telescope aperture.

II.A.3 Temporal Spectrum of Scintillation

The temporal spectrum can be derived from the spatial correlation function by use of Taylor's hypothesis of frozen turbulence. The assumption is that temporal variations are due to a wind translating a frozen turbulene past the telescope or interferometer. The validity of the hypothesis is discussed later.

The assumption of frozen turbulence greatly simplifies calculations relating spatial and temporal quantities. Equation II.13 relates the log amplitude at one point and time to another point downwind. This is Taylor's hypothesis. Equation II.14 follows immediately.

$$\chi(\vec{r},t) = \chi(\vec{r}+\vec{v}\tau, t+\tau) \qquad \text{II.13}$$

$$R_\chi(\tau) = B_\chi(v\tau) \qquad \text{II.14}$$

R is the temporal correlation

B is the spatial correlation

V is wind speed perpendicular to the line of sight

χ is the log amplitude

The frequency spectrum $F(f)$ of the intensity fluctuations is simply the fourier transform of $R_\chi(\tau)$. Using II.13 and II.14 we get eq. II.15.

$$F(f) = \frac{2}{\sigma_x^2} \int \cos(2\pi f t)\, B_x(vt)\, dt \qquad II.15$$

The integral in II.15 has been evaluated by Tatarski [13], who also derived expressions for the case where Taylor's hypothesis is not valid.

Experimental measurements of the frequency spectrum [25] at astronomical observatories, which cannot be directly compared with theory because temperature measurements are not available, show that the spectrum is flat out to ~100 Hz and then decreases rapidly . The modulation at 500 Hz is usually down several orders of magnitude. For horizontal propagation, where temperature measurements are available, agreement between theory and experiment has been mixed. For short path lengths theory and experiment agree [13]. For longer paths qualitative differences appear even when the scintillation is not saturated[26].

II.A.4 Strong Scintillation

Within the past several years, the theoretical problem of saturation of the variance of log intensity has been solved by a number of researchers[27-29]. While saturation does not occure for astronomical observations, the physical interpretation of one theory [27] is that saturation is due to a loss of spatial coherence of the wave front. This would imply that under scintillation saturation conditions, a high resolution

interferometer would not work even when signal to noise considerations are ignored. One experimental paper [30] showed the presence of phase discontinuities in the wavefront under strong turbulence conditions.

II.B Phase Fluctuations

Unlike scintillation which decreases with increasing telescope aperture, the effects of phase fluctuations become more important as the telescope aperture increases. For small telescopes, the image of a star is the telescope's diffraction pattern. The effect of turbulence is to cause the position of the image to wander randomly. As the the aperture is increased, the image begins to deviate from the diffraction pattern. For large telescopes, the image is a blur, which wanders randomly. While image blurring and image wander seem to be different phenomena, both are caused by phase fluctuations. Fluctuations of scale sizes smaller than the telescope aperture cause bluring while fluctuations larger than the telescope aperture produce image wander.

This section is a review of the study of phase fluctuations caused by atmospheric turbulence. The first subsection describes the phase structure function calculated using the Rytov method and other theoretical results. The relation of the phase structure function to image bluring, image wander, as well as the phase correlation length is discussed. The second subsection

discusses the time dependence of phase fluctuations. It has long been realized that the angular resolution of ground based instruments need not be limited to the size of the blur caused by turbulence. The third subsection reviews several techniques currently used to achieve diffraction limited performance, such as amplitude interferometery, speckle interferometery and active wavefront correction. So far, I have only discussed the distortion of a plane wave as it traverses the atmosphere. If an astronomical object has large angular dimensions, the light from one side of the object will distorted in a significantly different way than the light from the opposite side. The last subsection reviews the recent work on this problem often refered to as the isoplanatic patch problem.

II.B.1 Theory of Phase Fluctuations

The study of phase fluctuations in principle is very similar to the study of scintillation. However, several differences should be mentioned. Variations in the delay through the atmosphere are extremely large (10cm/C). At visible wavelengths the phase delay is meaningless. In fact, phase delay through the atmosphere is determined by weather conditions and gross motion of the atmosphere rather than turbulence. The study of phase fluctuations at optical wavelengths is therefore limited to phase

differences between points.

II.B.1.a Phase Structure Function

The function that is studied is therefore the phase structure function defined by eq. II.16.

$$D_\phi(r) = \langle [\phi(\vec{r}_1) - \phi(\vec{r}_2)]^2 \rangle \qquad \text{II.16}$$
$$r = |\vec{r}_1 - \vec{r}_2|$$

The probability distribution for phase differences, using the same arguements for scintillation, should be a normal distribution. However, in general, the phase differences are much larger than 2π and therefore the distribution modulo 2π will be almost uniform. The phase structure function has been calculated using the Rytov method[9]. Eq. II.17 is the expression for the structure function relevant to astronomical observations.

$$D_\phi(r) = 2.91\, k^2 r^{5/3} \int_0^L C_n^2(z)\, dz \qquad \text{II.17}$$
$$k = 2\pi/\lambda$$
$$L = \text{Length of turbulence}$$

II.B.1.b Applications of the Phase Structure Function

The importance of the phase structure function comes from the fact that it may be used to calculate a large number of parameters relevant to both imaging telescopes and stellar

interferometers. One application is to find the phase coherence length. The phase coherence length as defined by Fried [31] is the diameter of the telescope at which the RMS phase error averaged over the aperture is one radian eq. II.18.

$$\left\langle \iint dx\,dy\; A(x,y)\,(\phi(x,y)-\bar{\phi})^2 \right\rangle = 1 \qquad \text{II.18}$$

where A(x,y) is the aperture function

$A(x,y) = 1 \quad (x^2+y^2)^{1/2} < r$

$\quad\;\; = 0 \quad\;\; > r$

$\bar{\phi}$ is the average phase over the aperture

$\langle\ \rangle$ represents ensemble average

Fried [31] derived an expression for the phase coherence length r_o eq. II.19.

$$r_o = \left(\frac{6.88}{2.91\,k^2 \int C_n^2\,dz} \right)^{3/5} \qquad \text{II.19}$$

$k = 2\pi/\lambda$

A simple substitution of D_ϕ for $(\phi(x,y)-\bar{\phi})^2$ yields an expression similar to eq. II.19 except the constant 6.88 is replaced by 5.82.

Several properties have been shown to apply to the quantity r_o. The resolution of a long exposure photograph was shown to be equal to the diffraction limited resolution of a telescope with a diameter of r_o [31]. The average gain of an antenna for a static

optical heterodyne receiver could not exceed that of a receiver of diameter r_o in free space. An analysis of the geometry of the phase distortion [32] showed that the bulk of the phase distortion for small apertures was tilt. If the tilt is removed, the maximum effective aperture was 3.4 r_o [32] for a optical heterodyne receiver.

In terms of maximum effective aperture, the relation between an optical heterodyne receiver and a stellar interferometer is a close one. In a stellar interferometer, starlight from two spatially separated apertures are combined at a photodetector. For a heterodyne receiver, light from the external source is mixed with light from a laser at the photodetector. In both cases, the interfering wavefronts must be parallel across the sensitive area of the detector. For a stellar interferometer, both wavefronts are distorted by turbulence, while for a heterodyne receiver, the laser wavefront is plane. The maximum effective aperture for a stellar interferometer could be defined by eq. II.20.

$$\left\langle \iint dx\,dy\; A(\vec{r}) \left(\phi(r) - \phi(r+r') - \bar{\Phi} \right)^2 \right\rangle = 1 \qquad \text{II.20}$$

A(x,y) is the aperture function

r' is the baseline vector

$\bar{\Phi}$ is the difference of the average phases at the two apertures

For a long baseline interferometer, the fluctuations at the two apertures would be uncorrelated. Hence, the mean square phase difference is twice as large as for eq. II.18. Modifying eq. II.19 for this factor of 2 yields eq. II.21.

$$r_1 = \left(\frac{6.88}{2 \times 2.91 k^2 \int C_n^2 dz} \right)^{3/5} \qquad \text{II.21}$$

Since the interferometer has two apertures, the ratio of the maximum effective area for a heterodyne receiver and interferometer is eq. II.22.

$$\left(\frac{r_0}{r_1} \right)^2 = 1.15/2 \qquad \text{II.22}$$

The parameter r_1 is the maximum effective aperture for a static interferometer and $3.4 r_1$ for an interferometer with high speed angle trackers.

For ground to ground paths it is often possible to measure C_n^2. However, for astronomical measurements the maximum aperture must be determined by seeing measurements. Eq. II.23 defines the quantity "seeing" and eq II.24 is the expression derived in reference [31] relating seeing to r_0.

$$\text{Seeing blur} = 2\sigma_\alpha \sim 2\sqrt{\langle \alpha_x^2 \rangle} \qquad \text{II.23}$$

where α is the wavefront tilt

$$r_i = \frac{r_o}{\sqrt{1.15}} = \frac{17.2\,\lambda}{2\sigma_\alpha} \qquad \text{II.24}$$

r_o, r_i, in cm, λ in μ, $2\sigma_\alpha$ in arc sec

The quantity defined by II.23 is the diameter of the blur of a stellar image of a long exposure photograph taken with a small telescope. While precise seeing measurements have been made at a number of observatories, the seeing, as recorded nightly at individual telescopes is usually the diameter of the blur as seen by the astronomer through the telescope eyepiece. The diameter of a stellar image depends on the size of a telescope and the time constant of the detector. For a short exposure, wavefront tilt results in a translation of the image without bluring. As mentioned previously, phase fluctuations on a scale smaller than the telescope aperture causes bluring while fluctuations on a scale larger than the aperture cause image motion. Therefore, fluctuations which cause bluring on a large telescope cause image wander on a small telescope.

It has been shown [32] that the best short exposure resolution is obtained with a telescope of diameter 3.8 r_o where the resolution is equivalent to a telescope of 1.9 r_o in free space. For a long exposure image, image wander as well as image bluring will contribute to the degradation of the recorded image. The long exposure blur therefore should be independent of telescope size.

In the preceeding paragraphs, the words long, short, large

and small were undefined. It is possible to define these words in terms of r_o, the phase correlation length, L_o, the outer scale and the V, wind speed. Small apertures refer to apertures where wavefront tilt is the dominant form of wavefront distortion. Very large apertures refer to sizes comparable to L_o. Using Taylor's hypothesis of frozen turbulence, short exposures would imply a time scale of $< r_o/V$ and long exposures $> L_o/V$.

II.B.2 Temporal Structure of Phase Fluctuations

The derivation of the temporal spectrum of phase fluctuations is similar to the derivation for scintillation. Taylor's hypothesis is expressed as eq. II.25.

$$\phi(r,t) = \phi(r+v\tau, t+\tau) \qquad \text{II.25}$$

The temporal autocorrelation for phase is therefore eq. II.26.

$$R_\phi(\tau) = \langle \phi(r_1)\phi(r_2) \rangle \quad \text{where } v\tau = |r_1 - r_2| \qquad \text{II.26}$$

For many applications the quantity of interest is not $R_\phi(\tau)$ but the temporal autocorrelation of the phase difference at two points as defined by eq. II.27.

$$R_{\delta\phi}(\tau, r) = \langle [\phi(r_1,t) - \phi(r_2,t)][\phi(r_1, t+\tau) - \phi(r_2, t+\tau)] \rangle \qquad \text{II.27}$$

$$R_{\delta\phi}(\tau, r) = \frac{1}{2}\left[D_\phi(r - v\tau) + D_\phi(r + v\tau) - 2D_\phi(v\tau)\right] \qquad \text{II.28}$$

Tatarski [13] showed that this is eq. II.28.

Ground to ground measurements of $R_\phi(\tau)$ have been made [33] and these measurements are in good agreement with theory. There have been no measurements of $R_{\delta\phi}(\tau)$ that can be directly compared with theory.

Eq. II.28 is very closely related to the angle of arrival temporal autocorrelation. If a telescope is used to measure the angle of arrival, the measured quantity is the average tilt of the wavefront over the telescope aperture. If an interferometer is used to measure the angle of arrival, the measured quantity is the difference of the average phase at one aperture and the average phase at the second aperture.

A large aperture telescope measures the average tilt over a large area and hence the variance of the angle of arrival should be smaller. This is similar to the aperture averaging effect in scintillation. Unlike scintillation, which is correlated over 7-8 cm, phase fluctuations are correlated at great distances out to the outer scale of turbulence. The quantity r_o represents the distance at which the correlation is so high that phase differences are much less than a wavelength of light, hence r_o is a function of wavelength. The variance of the angle of arrival of a telescope as a function of diameter is given by eq. II.29

[13].

$$\langle \alpha^2 \rangle = \frac{D_\phi(r)}{k^2 r^2} \propto r^{-1/3} \qquad \text{II.29}$$

The reason the variance of the angle of arrival decreases so slowly with increasing aperture is because most of the fluctuations in the angle of arrival is caused by turbulence of very large scale sizes. As a result, the accuracy of astrometric measurements, if they are limited by atmospheric turbulence, would not improve dramatically with the use of larger telescopes.

The spatial averaging of a large telescope aperture becomes a temporal average when Taylor's hypothesis is applied. Hence, image motion is slower for a large telescope than a small telescope. For an interferometer, no spatial and hence no temporal averaging occures. The temporal autocorrelation of the angle of arrival of an interferometer is eq. II.30.

$$R_\alpha(r,\tau) = \frac{R_{\delta\phi}(r,\tau)}{r^2 k^2} \qquad \text{II.30}$$

II.B.3 High Resolution Instruments

Although work on a quantitative theory of atmospheric seeing did not begin until the 1950's, techniques to overcome the effects of turbulence date back to the 1860's when Fizeau [2]

suggested the use of a stellar interferometer to measure stellar diameters. At the present time a number of different methods are being used to overcome the effects of turbulence. While it is not practical to review all of the techniques that have been proposed to obtain high spatial resolution through the turbulent atmosphere, the three most widely used techniques, Michelson stellar interferometry, speckle interferometry, and real time phase correction will be discussed.

II.B.3.a Michelson Stellar Interferometer

Fizeau [2] was the first to suggest the use of an interferometer for measureing stellar diameters. The interferometer was a variation of Young's double slit interferometer. In 1874, Stephan [34] used a telescope as an interferometer by placing a screen with two holes in front of the telescope objective Fig. II.1. However, the baseline of his interferometer was insufficient to resolve any star. After some priliminary measurements with an interferometer similar to Stephen's, Michelson and Pease built the 20 foot interferometer shown in Fig. II.2. In 1921, they published the first measurement of a star's diameter [3] (other than the Sun).

Michelson's 20 foot interferometer was mounted on the 100 inch telescope on Mount Wilson. The light from the two entrance apertures were brought together at the focal plane of the telescope. If the pathlengths of the two interfering beams

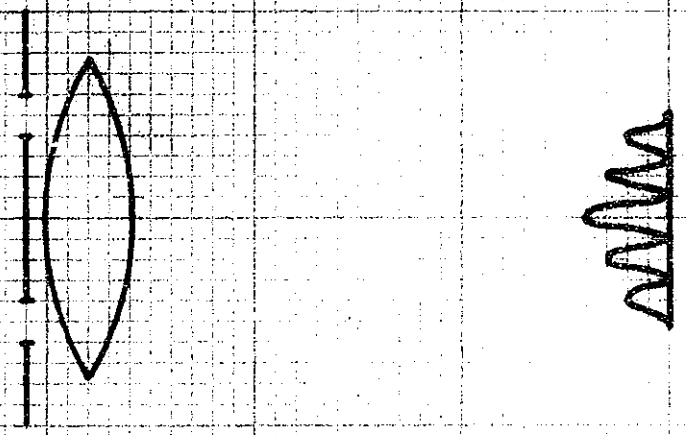

STEPHAN'S STELLAR INTERFEROMETER
(Similar to Young's Double Slit Interferometer)

FIG. II.1

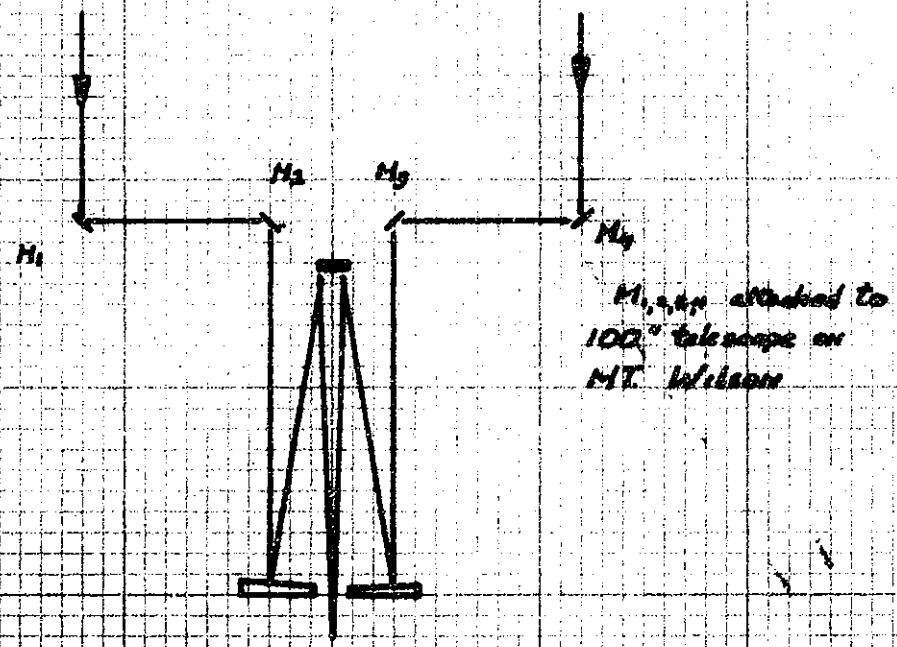

MICHELSON STELLAR INTERFEROMETER

FIG. II.2

differed by less than a few wavelengths, fringes would observed. The baseline was oriented in a north-south direction so that telescope drive errors would only produce a second order error in the relative pathlength of light. The fringe spacing is determined by the angle between the interfering beams according to eq. II.31.

$$S = \frac{\lambda}{\sin\theta} \qquad \text{II.31}$$

The quantity measured was the fringe visibility. The fringe visibility for an interferometer with a baseline D is the absolute value of the fourier component corresponding to the angular frequency D/λ cycles per radian. Michelson assumed that the star was a circular disk. Hence, the fringe visibility should have a minimum value at $D = 1.22\lambda/\theta$ where θ is the angular diameter of the star. The procedure for measuring the diameter of a star is to increase the baseline D until the fringes disappear.

Why doesn't the Michelson stellar interferometer suffer the same effects of atmospheric turbulence which plague ordinary telescopes? The reason is that the apertures were chosen to be smaller than $\sim r_o$ (defined in II.B.1.b) and phase distortion over each of the apertures is much less than λ. In addition the average phase difference (square root of the phase structure function) between the two apertures was sufficiently small for temporal coherence to be maintained.

In 1923, Pease began construction of a 50 foot interferometer. Two design changes between the 20 foot instrument and the 50 foot instrument resulted in an instrument that was much more difficult into operate (see Kababian [4]). Since the baseline of the 50 foot interferometer was oriented in a east-west direction, telescope drive errors had a first order effect on the relative path lengths rather than the second order effects of the north-south 20 foot interferometer. The 50 foot instrument also suffered a reduction in fringe visibility due to polarization effects. For stars at a declination of 45 the two images of the star that are superposed are rotated 90 degrees relative to each other, hence the fringe visibility would be zero.

The major difference between Michelson's 20 foot interferometer and Stephan's interferometer is the use of extension arms by Michelson to obtain a sufficiently long baseline to resolve Alpha Orionis. Interestingly several modern stellar interferometers are patterned after Stephan's interferometer rather than Michelson's, these include the interferometers built by Currie [35] and Low [36]. The different configurations for long baseline interferometers, interferometers not attached to existing telescopes, was studied by Kababian [4] and will be reviewed in chap 4.

II.B.3.b Speckle Interferometer

Speckle interferometry is a technique which obtains high spatial resolution information from the grains or speckles is a stellar image. A stellar speckle photograph is a short exposure photograph taken with a narrow bandpass filter. The stellar speckles are the same as laser speckles observed when a laser beam is reflected from a diffuse surface. Stellar speckles have been observed for some time, in particular, Debrus [37] in 1969 showed that the speckle pattern of a double star, two identical patterns laterally displaced, could be analyzed to measure angular separations smaller than the seeing blur. Labeyrie [38] devised a more general procedure for analysing speckle patterns.

The method measures the spatial power spectrum of an astronomical object. The speckle technique assumes that the speckle pattern may be expressed as a convolution of the object and a point spread function eq. II.32.

$$I = O \otimes G \qquad \text{II.32}$$

where O is Object's true irradiance distribution
I is the image at focal plane
G is Point spread function

Eq. II.32 is not always valid since it assumes that the field of view is within a single isoplanatic patch. This is discussed in greater detail in (II.B.4) The fourier transform of eq. II.32 is eq. II.33.

$$\tilde{I} = \tilde{O}\,\tilde{G} \qquad \text{II.33}$$

$\sim$ denotes fourier transform

It is well known that the resolution of a long exposure

$\langle I(x,y) \rangle$ is limited by turbulence. Labeyrie's technique is to average the power spectra $\langle |\tilde{I}|^2 \rangle$ rather than the image. For normalization purposes, the average power spectrum of an unresolved star must also be recorded, although not at the same time. The power spectrum of the object is expressed in eq. II.34.

$$\frac{\langle |\tilde{I}|^2 \rangle}{\langle |\tilde{I}_p| \rangle} = \frac{|\tilde{O}|^2 \langle |\tilde{G}|^2 \rangle}{|\tilde{O}_p|^2 \langle |\tilde{G}|^2 \rangle} = |\tilde{O}|^2 \qquad \text{II.34}$$

Since the images of the target star and the reference star are not recorded simultaneously, it is necessary to assume that $\langle |\tilde{G}|^2 \rangle$, the time averaged power spectrum of the telescope and atmosphere impulse response is constant. The speckle processing procedure is usually implimented with a coherent optical analog computer. Several digital signal processors have also been built [39].

Because of the ease of speckle interferometry relative to other spatial interferometers, the technique has been extensively studied. The function $\langle |\tilde{G}|^2 \rangle$. has been calculated, assuming a Kolmogorov turbulence spectrum, and using the Rytov method [40]. At high spatial frequencies, the function has the form of eq. II.35.

$$\langle |\tilde{G}|^2 \rangle = \frac{1}{N} \langle |\tilde{G}(0)|^2 \rangle T_o(f) \qquad \text{II.35}$$

N is the average number of speckles or $A/\pi(r_o/2)^2$

where A is the area of the telescope

$T_o(f)$ is the optical transfer function of the telescope

(fourier transform of a point diffraction pattern)

In addition the signal to noise ratio R at low light levels has been calculated [41] to be eq. II.36.

$$R(f) = \frac{N_s \, T_o(f)}{1 + N_s T_o(f)} \sqrt{N_i} \qquad \text{II.36}$$

Ns = average number of photons detected per speckle

Ni is the number of speckle pictures averaged

From eq. II.36, we see that even at high light levels, a moderate number (50-100) of speckle pictures are necessary to average out the "atmospheric" noise. At low light levels the signal to noise ratio is proportional to the average number of photons per speckle (not the square root of the number). This is the same as for the intensity interferometer of Brown and Twiss (see II.B.3.d).

This may understood with the following arguement. If only one photon is detected in the image of a double star, the only information we can deduce is that one star exists. The angular separation of the double star can be estimated only if two or more photons are detected. To generalize, in determining the shape of an object, the signal to noise ratio is proportional to the square root of the fraction of speckles for which two or more photons have been detected. When the average number of detected photons per speckle is less than one the vast majority of speckles will have 0 or 1 detected photons and hence be useless in determining the shape of the object. For very low light levels, the probability of detecting 3 or more photons per speckle is negligibly small and the signal to noise ratio is proportional to the photon flux eq. II.37.

$$R \propto \left[\frac{N^2 e^{-N}}{2!}\right]^{1/2} \sim N\sqrt{1/2}$$

the quantity inside [] is the poisson probability for detecting two photons.

II.B.3.b.1 Variations of the Speckle Technique

In the recent past, numerous [42] techniques have been proposed to extract phase and not just power spectra information from the speckle pattern. The measurement of phase is qualitatively different from amplitude or power measurements. If the phase error due to photon noise is greater than 2π in a

single speckle photograph, it is no longer possible to increase the accuracy of the phase measurement by averaging a large number of independent measurements.

Since the speckles are a result of interference effects, temporal coherence conditions must be met. Most speckle observations with large telescopes use narrow bandwidth filters, 100 Å to 250 Å wide, to maintain temporal coherence. The narrow band widths are necessary because of the path length errors produced by turbulence. If the speckles were visible in white light, the sensitivity of speckle imaging techniques would be enhanced. Speckle processing of the output of a real time phase compensation system, used not to produce diffraction limited images but to maintain temporal coherence, would be a way of obtaining the advantages of both active and passive systems.

II.B.3.c Real Time Phase Compensation

All the high resolution techniques described so far are passive measurement systems. Since the low resolution of ordinary telescopes are primarily caused by phase front distortion, phase compensation would result in a diffraction limited image. This was first suggested by Babcock in 1953 [43].

A real time phase compensation system consists of a wavefront sensor, a wavefront corrector, usually a "rubber" mirror, and a control system which uses the wavefront sensor data to actuate the wavefront corrector. Since the phase correlation

length r_o is typically 10 cm a large telescope such as a 5 meter telescope would require thousands of correcting elements. The components necessary to build a phase compensation system has only recently become available. In many cases, the technology for the components was developed as the need arose. Because of the complexity and cost of a phase compensation system, most of the research has been conducted outside of the astronomy community.

The advantage of phase compensation over passive "speckle" imaging is that the optical bandwidth of the detectors need not be limited to 100-200 $\mathring{A}$ since temporal coherence is maintained by a servo. The disadvantage of most phase compensation systems is that diffraction limited images are achieved only if the residual phase front errors are less than 0.1λ . This would require the phase front measurement system to be much more accurate than 0.1λ for any realizable control system. Since the accuracy of the wavefront sensor is photon noise limited, the sensitivity of an active system is degraded by an amount that is the difference between the measurement error and servo control error.

Dozens of phase compensation systems have been proposed. Successful operation of two image sharpening systems on small telescopes have been reported [44,45]. There is little doubt, given the enormous research effort in this area, that diffraction limited imaging on large telescopes will be achieved, at least for bright stars.

Both phase compensation and speckle imaging are severely

limited by two constraints. The first is sensitivity, which would probably be highest for a combined active-passive system. However any phase measurement system is probably limited to ~10 mag stars. The second limitation is the isoplanatic patch limitation (see II.C) which limits the field of view to a few arc seconds.

II.B.3.d Narrow Bandwidth Instruments

The high resolution instruments described in the previous three subsections are all mechanically precise instruments. Mechanical precision is required because temporal coherence must be maintained. Another way to maintain temporal coherence is to use a detector with a very narrow effective optical bandwidth. Two examples of narrow band optical interferometers are the Hanbury Brown and Twiss intensity interferometer [46] and the infrared heterodyne interferometer [47].

The arguement for developing a narrow band interferometer is that the high mechanical precision (20 micron) of passive interferometers, and the very high precision (0.1 micron) of phase compensation systems cannot be achieved for a long baseline interferometer. While this was true in the 1950's when the intensity interferometer was first proposed, many scientists do not share this opinion at the present time.

For temporal coherence to be maintained, $\Delta L \Delta \nu$, the product of the pathlength difference between the interfering beams and the optical bandwidth, must be less than C. For both the

intensity interferometer and the heterodyne interferometer, ΔL is a few centimeters and is determined by instrumental uncertainties such as the length of the coaxial cables and the position of the telescopes rather than by atmospheric turbulence. $\Delta\nu$ is limited by the electrical bandwidth of the detectors (photodiode and photomultiplier) rather than the ΔL of the instrument. Despite the great historical importance of the intensity interferometer, the following discussion of narrow band interferometers will be brief.

The intensity interferometer was first proposed as a radio interferometer [48] to overcome the problem of variations in cable delay. Later, [46] Brown and Twiss showed that the intensity interferometer should work in the visible (Fig. II.3). The correlation of photon arrivals at two detectors from a coherent source (both spatially and temporally) was a controversial topic in 1958.

Let the intensity of light at one telescope be I (t) and define the fluctuations in intensity by eq. II.38.

$$\Delta I_1 = I_1(t) - \langle I_1(t) \rangle \qquad \text{II.38}$$

Brown and Twiss [46] showed that the correlation function of the fluctuations was the square of the mutual coherence. If temporal coherence is maintained, the correlation is the square of the spatial coherence (square of Michelson's fringe visibility) eq. II.39.

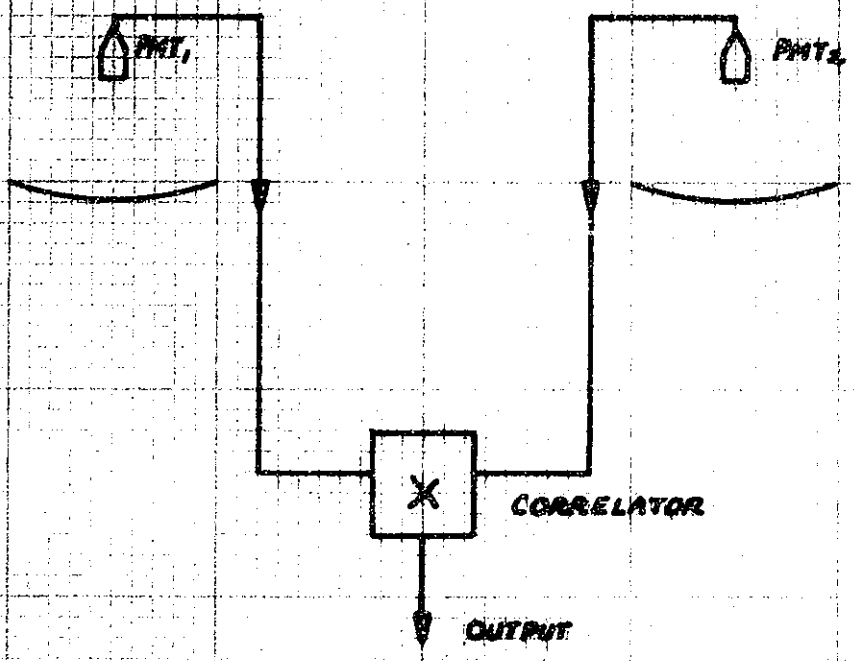

FIG. II.3 BROWN-TWISS INTENSITY INTERFEROMETER

$$(\text{Fringe Amplitude})^2 = \langle \Delta I_1 \, \Delta I_2 \rangle \qquad \text{II.39}$$

The effective optical bandwidth is the same as the electrical bandwidth of the system which is limited by the electrical bandwidth of the detector (~1 GHz). Because of the high gain and low noise of the electron multiplier in the phototubes, the system was photon noise limited.

The infrared heterodyne interferometer [47] is very similar to a radio interferometer. Stellar radiation is mixed with the local oscillator (a CO2 laser) on the face of a photodiode. The two local oscillators for the two telescopes are phase locked. The down-converted signals from the two telescopes are amplified and processed in the same way as in a radio interferomter. The instrument can measure phase, and amplitude and can also be used as an intensity interferometer.

The ouput of the photomixer is proportional to the product of the stellar field and the local oscillator field. By using a high power local oscillator, the photomixer output can in theory, be increased to the point where the dominent noise source of the system is stellar photon noise. The effective optical bandwidth is limited by the photomixer (1 GHz) [49]. Because a heterodyne receiver is capable of near photon noise limited operation in the infrared, the huge difference in the bandwidth between a heterodyne interferometer and an ordinary Michelson interferometer does not accurately reflect the relative

sensitivity of the two instruments.

However, the relative sensitivity of a visible wideband interferometer versus a heterodyne interferometer is easily calculated from bandwidth and quantum efficiency data. The wide band instrument is more sensitive by aproximately $6.*10^5$.

II.C Isoplanatism

As mentioned earlier, the field of view of speckle and many other high resolution techniques is limited to typically a few arc seconds. Because of the superposition priciple, it is possible to express the image at the focal plane of a telescope as eq. II.40.

$$I(u) = \int O(u')\, G(u,u')\, du' \qquad \text{II.40}$$

I = image after distortion
O = true object irradiance

where G is the atmosphere-telescope Green's function

If the Green's function is shift invariant, eq. II.40 becomes a convolution. This is the assumption of speckle interferometry (eq. II.32), and other high resolution techniques. The isoplanatic patch is the area over which the green's function is shift invariant.

If atmospheric turbulence were concentrated at a single thin layer near the telescope, the whole sky would be isoplanatic. In reality, turbulence exist throughout the troposphere up to an altitude of 10 Km or more. Isoplanatism has been studied by a

number of researchers [50-52]. Several different approaches to the subject have been taken.

One approach is to quantify the degree of isoplanatism, in terms of the loss of high resolution information as the field of view is increased, or in terms of the correlation of the irradiance patterns of two stars as a function of the angular separation of those two stars[52]. For a telescope with a diameter less than r_o the resolution is limited by diffraction ard not atmospheric turbulence hence the whole sky is isoplanatic.

If we only consider large aperture instruments ($>>r_o$), isoplanatism can be defined in the following way. Consider a point source on the ground. A spherical wavefront is emitted. The wavefront is progressively distorted by turbulence until the wavefront is above the atmosphere. The size of the isoplanatic patch can be defined as the solid angle over which the rms wavefront distortion is 1 radian or less. Using a similar definition, Shapiro [51] has calculated the size of the isoplanatic patch to be eq. II.41 for vertical propagation.

$$\text{Solid Angle} = \frac{\pi}{3}\frac{r_o'^2}{H^2} \qquad \text{II.41}$$

H is the effective height of turbulence

r_o' is the spherical wave equivalent to r_o defined by eq II.19 for a plane wave.

$$H^2 = \frac{\int C_n^2 z^2 \, dz}{\int C_n^2 \, dz} \qquad \text{II.42}$$

$$r_o' = \left(1.09 \left(\frac{2\pi}{\lambda} \right)^2 \int C_n^2 \, dz \right)^{-3/5} \qquad \text{II.43}$$

If we assume H=10 Km , r_o =0.1 m, the diameter of the patch is 2.5 arc sec. Note that since r_o' increases with increasing wavelength the isoplanatic patch also increases with wavelength.

III Conventional Astrometry

Astrometry, the oldest branch of astronomy, has been studied for over two thousand years. In the past, significant advances in astrometry instrumentation, such as the invention of the telescope and the use of photographic film have resulted in new discoveries. The purpose of this chapter is to review the current state of astrometric instruments and to provide a historical background for the astrometric interferometer.

III.A Conventional Instruments

A large number of astrometric instruments are currently in use. These instruments fall into two catagories. The first catagory includes instruments such as transit telescopes, zenith telescopes, and astrolabes. These instruments are used for absolute astrometry, relating the position of stars to the earth's rotation axis. Instruments in the second catagory are used for relative astrometry. While absolute astrometry is an important part of astrometry, this review will concentrate on relative astrometry instruments since the astrometric interferometer can only make relative measurements.

For many decades after the turn of the century, the primary astrometric instrument was the long focus camera. The use of long focus refracting telescopes was due to the work of Schlesinger

[53] who analyzed the errors in the instrument and devised methods in both data collection and analysis to minimize these errors. In more recent times, astrometric telescopes have been built using moderate aperture (>1 meter) reflectors instead of small refractors[54].

In the late 1960's photoelectric astrometric instruments were proposed to replace photographic instrument. This was in part a response to the measurement of solar oblateness by Dicke [55]. The subsequent measurement of solar oblateness by Hill et. al. [56] was qualitatively different from Dicke's original measurement. The goal of the photoelectric instruments such as SCLERA is to achieve astrometric accuracies limited only by atmospheric turbulence. The next two sections of this chapter will describe first the systematic errors of photographic instruments and second the ultimate performance of photoelectric instruments.

III.B Systematic Errors in Photographic Astrometry

In photographic astrometry, the position of stars are determined by measuring the position of stellar images on a plate. Corrections are made for tangent plane distortion and abberations in the optics. Errors due to mechanical flexure are minimized by taking all photographs of a star only over a narrow range of hour angles usually near transit. While it is not possible to list all possible sources of systematic error, the

more important ones will be mentioned.

The magnitude error is caused by telescope guiding errors. If the tracking is not perfect, the star's image will be smeared, usually in an asymmetric manner. This blur should be identical for all the stars on the plate. While the relative positions of the centroids of the blurs would remain constant if a linear detector is used, photographic film is logarithmic detector. As a result, the measurements of an astrometric plate where the intensity of the target star has been attenuated to the same magnitude of the reference stars is more accurate than a normal photograph such as a Palomar Sky Survey plate. On reflecting telescopes, coma produces an asymetric image and as a result produces an offset in the star's position which is dependent on the position of the star in the field of view and the magnitude of the star. Typical errors from the magnitude effect are 0.1 arc sec per magnitude if left uncorrected.

A second source of error is emulsion shift. The gelatin in which the silver grains are embedded is soft during film development and the amount of shift depends on a large number of variables such as the angle at which the plate was held when it was dried. Although this source of error may be as large as 0.02 arc sec [57], the effect is small and was not noticed for many decades of photographic work. A number of techniques are used to minimize the error due to emulsion shift. A common technique is to take multiple exposures of the same star field with the same photographic plate in different orientations.

A third source of error is caused by chromatic effects. Chromatic effects arise from atmsopheric dispersion as well as dispersive effects in refracting telescopes. Stars of different spectral type will suffer different amounts of refraction by the atmosphere. To make matters worse, most photographic plates are more sensitive in the blue region of the spectrum where the atmospheric dispersion is greatest. To minimize chromatic effects, astrometric photographs are taken through a narrow band pass filter, usually 600 Å wide centered at 5600 Å [58]. In addition, the reference stars are usually chosen to approximate the color of the target star. As an example of the size of this effect, a shift of the effective wavelength of 50 Å for a star 20 degrees from the zenith would produce an error of 0.036 arc sec.

Differential atmospheric refraction is also a potential source of error. For a 0.5 degree field of view, the effect is approximately 0.5 arc sec (near zenith). Typical day to day changes in the pressure of 4% would produce astrometric errors of 0.02 arc sec. However, modern data analysis techniques use a large number stars to model the distortion of the atmosphere caused by major weather patterns.

Until about a dozen years ago, the positions of stellar images were measured by hand and this was considered a significant source of error. With automatic laser monitored measuring engines, this source of error has almost disappeared.

III.C Ultimate Accuracy of Conventional Instruments

The discovery and elimination of systematic errors in photographic astrometry made it possible to average years of data to increase accuracy. To futher increase accuracy, many observatories began extended observing programs averaging data taken over a period of decades. The study of systematic errors became even more important since the usefulness of decades of data depends on the understanding and elimination of systematic errors.

In the late sixties, another approach to high accuracy was proposed. The goal was to construct a photoelectric astrometric instrument whose accuracy was limited only by atmospheric turbulence and hence achieve 0.001 arc sec accuracy in days to weeks of observation instead of years and decades of observation. One such instrument SCLERA has been built [59], and has been used primarily for solar oblateness measurements. This section estimates the ultimate performance of a turbulence limited instrument, for comparison with the astrometric interferometer.

Turbulence limited instruments such as SCLERA eliminate known systematic errors in a number of ways. Mechanical errors are eliminated by positioning the telescope permanently in a vertical position and using alt-az siderostat or heliostat mirrors to direct the light into the telescope. Thermal effects are minimized by using low expansion materials and placing the telescope in a temperature controlled enviorment. A photoelectric detector on an interferometric measuring engine is used in place of the photographic plate eliminating the magnitude error and

emulsion shift error. Chromatic effects are minimized by using narrow bandpass filters and recording the spectrum of the stars. Differential refraction can be minimized by measuring the local pressure, temperature and humidity (or local index of refraction of air). In addition, SCLERA is enclosed in a vacuum system, including siderostat mirrors.

Before evaluating the performance of a turbulence limited instrument, we will difine the following quantities.

$$\vec{\alpha}(t) = \alpha_x(t)\,\hat{x} + \alpha_y(t)\,\hat{y} \qquad \text{III.1}$$

α is the apparant position of the star

$$R_{\alpha_x}(\tau) = \langle \alpha_x(t)\,\alpha_x(t+\tau) \rangle \qquad \text{III.2}$$

R is the temporal autocorrelation function

<> denotes ensemble average

For a measurement of duration T, the expected error in one coordinate due to atmospheric turbulence defined by eq. III.3.

$$\sigma_{\alpha}(T) = \left[\left\langle \frac{1}{T} \left(\int_0^T \alpha_x(t)\,dt \right)^2 \right\rangle \right]^{1/2} \qquad \text{III.3}$$

This may be rewritten as eq. III.4.

$$\sigma_{\alpha_x}(T) = \left[\frac{1}{4T^2} \int_0^T dt_1 \int_0^T dt_2 \; R_{\alpha_x}(t_1 - t_2) \right]^{1/2} \qquad \text{III.4}$$

Since phase fluctuations are correlated over distances out to the outer scale of turbulence, each measurement of duration T is not independent of other such measurements unless T>TO, where TO is the wind speed divided by the outer scale. For measurement times much longer than TO the error will decrease as $\sqrt{T}$.

The integral in eq. III.4 was evaluated numerically using measurements of R_{α_x} from Wallace Observatory (see Chap 6). The accuracy of a one second measurement at Wallace Observatory was 1.6 arc sec for 4.5 arc sec seeing. However, for relative astrometry over a small field of view, a part of the image motion will be correlated over the whole field of view. Kolchinskii [60] has studied the correlation of image motion and found a 50% correlation for stars separated by 10 arc min. Hence the accuracy of relative astrometry for 4.5 arc sec seeing is 0.8 arc sec for a one second measurement in a 10 arc min field. For 1 arc sec seeing, the accuracy would be 0.18 arc sec and 0.001 arc sec accuracy would require 9 hr of observation. For 2 arc sec seeing 36 hours would be necessary.

Accuracies of 0.03 arc sec in 4 min of observation with SCLERA has been reported for a 0.5 degree field of view and 2 arc sec seeing. This is close to the estmate in the preceeding paragraph (0.03 arc sec in 2.4 min). At much higher accuracies, SCLERA is limited by systematic errors and not turbulence.

Probable errors of 0.012 arc sec were reported [56] for solar oblateness measurement after 12 days of observation. However, a major part this error was due to the difficulty of measuring an edge of the sun, and the possibility of excess equatorial brightness. Stellar measurements would probably be more accurate.

III.D The Accuracy of Conventional Instruments

The random and systematic errors which limit the accuracy of conventional instruments has been reviewed. However, even if all known systematic errors are corrected to 0.001 arc sec and random errors are below 0.001 arc sec the true accuracy of a measurement may be significantly worse than 0.001 arc sec.

Analysis of photographic data has shown that the achievable accuracy for one night of observation is limited to 0.02 arc sec[61] independent of the number of plates taken. This was calculated by comparing data from photographs of the same star field with the same telescope taken over a period of years. The same study showed that a yearly limit of 0.002 arc sec also exists. Unfortunately, most of the historical data used in this analysis did not include local weather information (see III.B atmospheric refraction) and more recent photographic measurements may be more accurate.

In the measurement of parallax by photographic astrometry, the relative parallax of the target star is determined by the

motion of the target star relative to background or reference stars. The motion is an elipse. Measurement of either the major or minor axis of the eslipse is sufficient to determine the parallax. Comparing the two determinations provides a check on the consistancy of the data. Typical errors are 2-3 x 10^{-3} arc sec for parallax deterinations involving several years of data.

These estimates of the accuracy of photographic astrometry, internal consistancy of data taken at a single observatory, are quite different from the estimates of external errors, errors calculated by comparing data from more than one observatory. Vaselevskis [1] in the early 1960's compared the parallax determinations from 6 observatories. The differences averaged (rms) 0.018 arc sec significantly larger than the 0.002 to 0.003 arc sec internal agreements. The differences between repeated measurements at the same observatory were only slightly better. A more recent study (1976) [62] of external errors in the General Catalog of Trigonometric Parallaxes (1963) reports the mean error to be 0.016 arc sec.

In conclusion, the accuracy of photographic techniques could be anywhere from 0.002 to 0.016 arc sec. For a few isolated cases such as Barnard's star the lower number may be correct, although measurements at Allegheny [63] do not confirm the measurements at Sproul [64]. Photoelectric instruments are probably much more accurate but at the present, SCLERA, the only photoelectric instrument is not conducting a parallax program.

IV Astrometric Interferometer

In chapter three we saw that the accuracy of modern astrometric instruments now approach the limit imposed by atmospheric turbulence. However, a number of instruments (II.B.3) are capable of overcoming the deleterious effects of the atmosphere. It is therefore only natural to try adapt a high resolution instrument for astrometry. The idea for using a Michelson stellar interferometer for astrometry probably dates back to Michelson. However, serious attention has not been given to an astrometric interferometer for a number of reasons. First, long baseline interferometers are difficult to build because of the requirements of temporal coherence. The most serious problem however, was the isoplanatic patch problem discussed in section II.C.

This chapter describes an astrometric interferometer that theoretically can achieve 10^{-4} arc sec accuracy. The first section describes the principles of the astrometric interferometer. This includes the detection and measurement of fringe position at low light levels, astrometry with interferometers, and the two color technique for correction of nonisoplanatic errors. The second section discusses the limitations imposed on the operations of the astrometric interferometer by atmospheric turbulence. The magnitude limit and accuracy of the astrometric interferometer are estimated. The third section is a brief analysis of the major systematic

errors of an astrometric interfereomter. The errors from the laser reference interferometer, the calculation of baseline coordinates, and the instabilities of the pedestals are analysed.

IV.A Principle of the Astrometric Interferometer

IV.A.1 Fringe Detection and Position Measurement

A simplified optical schematic of an astrometric interferometer is shown in fig. IV.1. Star light entering the instrument at two entrance apertures, are linearly added at the beam splitter. The output of the beam splitter is then focused onto a photomultiplier. If we assume the star is an unresolved spatially coherent source, the photocurrent from the photomultiplier will only be a function of the path length difference τ, between the two interfering beams. For starlight, which is not monochromatic, the detector output as a function of τ ,delay, is the fourier transform of the spectrum eq. (IV.1).

$$I(\tau) = \int I(\nu) [\cos \nu\tau + 1] \, d\nu \qquad \text{IV.1}$$

$I(\nu)$ is the spectrum of the star

From eq. IV.1 we see that the detector output is a maximum if the quantity $\tau = 0$. In addition if I(v), the spectrum of the star, is

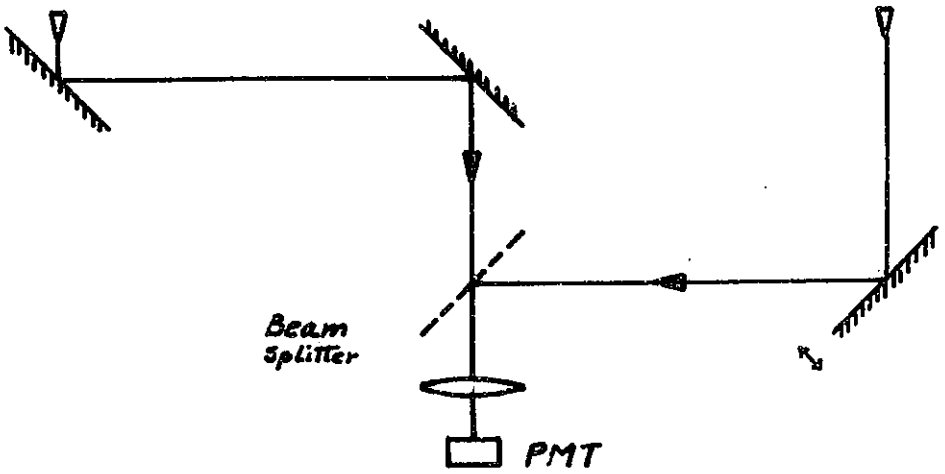

Fig IV.1

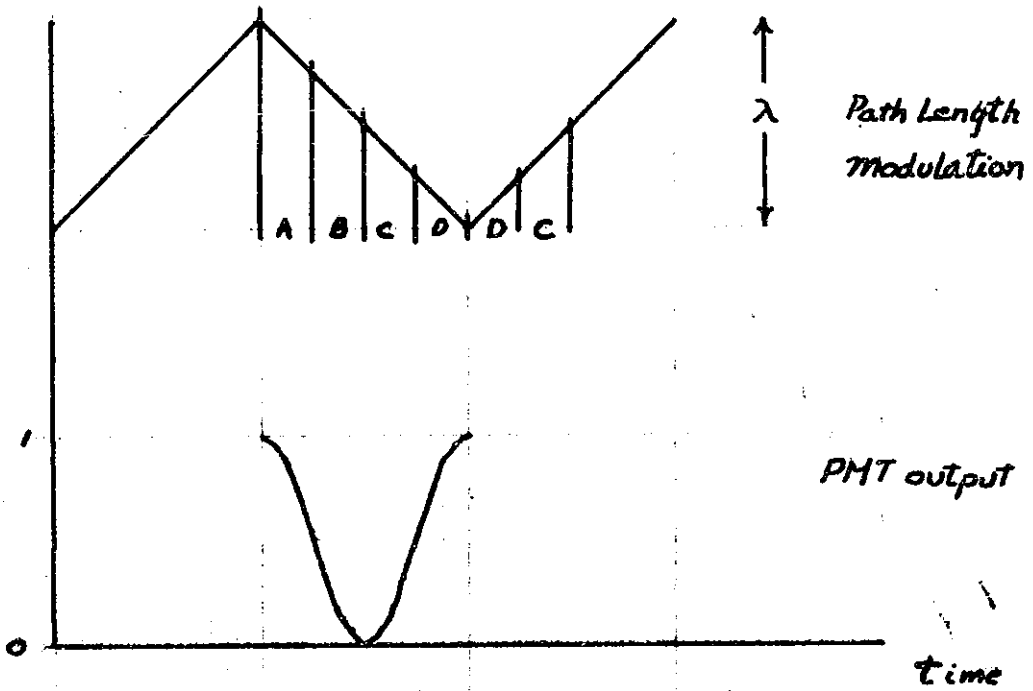

Modulation Pattern for Fringe Detector

Fig. IV.2

centered around ν_o then the output would have other maxima at $\tau = n*c/\nu_o$, and would have minima at $\tau = (n+1/2)*c/\nu_o$, where n is an integer. The central maxima or central fringe would be the largest. The position of the central fringe of a star, which depends on the position of the star and the orientation of the baseline, can be defined as the position of the programmable delay line that results in the maximum detector output.

In practice it is extremely difficult to position the delay line with a servo system to the center of the fringe to within a small fraction of a wavelength. However, as long as the positioning error (servo error) is known, the size of the positioning error is unimportant. The achievable accuracy is therefore determined by the noise in the measurement of the servo error.

A method for tracking fringes is the following. The path length in one arm of the interferometer is modulated by a triangle wave with peak to peak amplitude λ. Each sweep of the modulator is divided into four intervals, and the number of photons detected during these intervals, i.e., A, B, C, D, is used to estimate the intensity of light, N, the photon noise level, the fringe visibility V, and the fringe phase , eq. IV.2 to IV.4.

$$N = A + B + C + D \qquad \text{IV.2}$$

$$V = \frac{\sqrt{2}}{N} \pi \left[(A-C)^2 + (B-D)^2 \right]^{1/2} \qquad \text{IV.3}$$

$$\Phi = \text{Tan}^{-1} \left[\frac{A-C}{B-D} \right] + \frac{\pi}{4} \qquad \text{IV.4}$$

The measurement of fringe phase must be made on a time scale sufficiently short to freeze atmospheric turbulence (10 msec). The need to make phase measurements on a short time scale sets a stellar magnitude limit for this type of instrument (see IV.B.1).

IV.A.2 Astrometry with an Interferometer

If we assign the value 0 to the position of the central fringe when the star's position is perpendicular to the baseline, eq. IV.5 then defines the relation between the fringe position and the star's position and the baseline length and orientation.

$$\text{Fringe Position} = \hat{S} \cdot \vec{B} \qquad \text{IV.5}$$

$\hat{S}$ is a unit vector to the star

$\vec{B}$ is the baseline vector

A single measurement of the fringe position would not be sufficient to determine the position of a star since $\hat{S}$ contains

two independent variables. If the baseline vector were always known, two measurements of the fringe postion at two different baseline orientations would be sufficient to determine the coordinates of the star. In general, however, neither the baseline nor the star's position are known relative to an inertial reference frame. Hence the absolute position of a star may not be determined without additional information. If we make simultaneous measurements of the fringe positions of a number of stars, it is then possible to determine the relative positions of the stars. Each measurement of a fringe position of star i at the j'th baseline is represented by eq. IV.6. Each star represents two unknowns, and each new baseline orientation represents 2 new unknowns. The total number of baseline unknowns is 2j-3. In order to find the relative positions of the stars the number of measurements must be larger than the number of unknowns. This is represented by eq. IV.7.

$$\text{Measurement}_{ij} = \hat{S}_i \cdot \vec{B}_j \qquad \text{IV.6}$$

$$i \cdot j \geq 2i + 2j - 3 \qquad \text{IV.7}$$

It is impossible to measure the fringe position of i stars simultaneously with one interferometer. A switching scheme must therefore be used to make quasisimultaneous measurements.

Optical interferometric astrometry is similar to radio VLBI

(very long baseline interferometry) astrometry. The most important difference is that radio VLBI uses very long baselines and are much less sensitive small lateral displacements of the collecting apertures. For example, 10^{-4} arc sec times 5000 km is 2.4 mm while 10^{-4} arc sec times a 10 meter optical baseline is 5 nanometers. In radio VLBI, it is possible to model baseline motion with earth rotation and solid earth tide. In the optical, the baseline as determined by the position of the end mirrors must be measured to very high accuracy (see sec. IV.C.2).

IV.A.3 Correction of Nonisoplanatic Errors

The measurement of fringe phase that was described in IV.A.1 yields the fringe position after the light has traversed tens of kilometers of atmosphere. While the average atmospheric refraction near zenith may perhaps be calculated to 10^{-4} arc sec accuracy with the use of meterological data, the fringe position caused by turbulence still persists. If a simultaneous differential fringe position measurement were performed between two stars, the isoplanatic limitations would restrict the field of view to a few arc seconds. If high accuracy for large fields of view is achieved by averaging the turbulent motion, this atmospherically limited performance would be approximately the same as for the other photoelectric astrometric instruments such as SCLERA, which was mentioned earlier. This problem can be bypassed as follows.

By measuring the fringe position at two bandpasses centered at λ_1 , λ_2 (0.4, 0.65 um) and using the known dispersion of the atmosphere, we can calculate the zero atmosphere fringe position P_o eq. IV.8

$$P_o = P_1 - (P_1 - P_2)\left[\frac{1-n_1}{n_2-n_1}\right] \qquad \text{IV.8}$$

n_i is the index refraction at λ_i

P_i is the corresponding fringe position

P_o is calculated for each 10 ms period and then averaged. The importance of averaging P_o, a quantity with an accuracy limited by photon statistics but not atmospheric statistics, cannot be overstressed. This is the essence of the astrometric interferometer technique.

That the two color correction scheme should work can be understood by considering two rays from an unresolved star. Each ray, defined by a trajectory everywhere perpendicular to the isophase surface with a 12 cm aperture, executes a random walk, the optical length which is determined by the geometry of the path and the average refractive index along the path. Fortunately it is the average refactive index that dominates the path length, and not the geometric effects. A reasonable geometric effect, under good seeing conditions, would result from two atmospheric lenses with a 1 arc sec deflection, one at the surface and one at 10 km altitude. This would lengthen the path by (1-cos 1")x10 km=

0.1 um or 0.2 wavelengths. A typical large wedge of air producing a 1 arc sec deflection, however would contribute (sin 1")x10 m= 48 um or 100 wavelengths by refractive effects. This random contribution to differential pathlength is the dominant one that actually limits the performance of conventional astrometric systems. Because it arises from variations in the index of refraction it can be corrected by the two color procedure.

In eq. IV.8 the factor F as defined by eq. IV.9 may be viewed as the normalized spectral dependence of the index of refraction of air and is essentially independent of temperature and pressure.

$$F = \frac{1 - N_1}{N_2 - N_1} \qquad \text{IV.9}$$

Although a change in the composition of the atmosphere could alter F, in practice even large changes in humidity would not be significant.

If the factor F in eq IV.8 is unknown, it may be derived in the following way from the data. Two consecutive 10 msec measurements yield eq. IV.10.

$$P_o = P_1 - (P_1 - P_2)F$$
$$P_o = P_1' - (P_1' - P_2')F \qquad \text{IV.10}$$

$P_{1,2}$ are the measurement at the first 10 msec period

$P'_{1,2}$ are the measurement at the second 10 msec

We see that, if we correct for earth rotation so that the true fringe position is constant in time, two consecutive 10 msec

measurements yield two equations in two unknowns. Since F would normally be stable for a much longer period than 20 msec, a least squares procedure should be used to evaluate both F and the true stellar fringe position.

At large zenith angles, the dispersion of the atmosphere will produce a spatial displacement of the two colors. When this displacement is larger than the isoplanatic patch ($za \geq \sim 45^{\circ}$) the two color technique will not work.

IV.B Atmospheric Constraints

Although the astrometric interferometer overcomes many of the atmospheric limitations of conventional astrometric instruments, the operation of the astrometric interferometer is still severely limited by the atmosphere. This section discusses two limitations, magnitude limit and achievable accuracy.

IV.B.1 Magnitude Limit

The fringe phase must be measured on a time scale sufficiently short to freeze atmospheric turbulence. In addition, the measurement error must be significantly less than 2π, otherwise it will be impossible to determined which fringe is being tracked. These two conditions set the stellar magnitude limit of the instrument.

Errors in the estimate of ϕ are primarily due to photon

statistics. While scintillation does not bias ϕ, it does increase noise in two ways. First, during scintillation nulls, the signal to noise ratio is decreased. The second and more serious effect is that light from the two apertures scintillate independently thereby reducing fringe visibility. For the fringe detection method discussed in IV.A.1 the rms phase error $\Delta\phi$ is approximately eq. IV.11.

$$\Delta\phi = \frac{1}{V} \frac{\pi}{2} \sqrt{\frac{1}{N}} \qquad IV.11$$

V is the fringe visibility

N is the average number of detected photons

From eq. IV.11 we see that the limiting magnitude depends on the average number of detected photons per interval of time during which the atmosphere can be considered frozen. The limiting magnitude is therefore determined by the size of the interferometer apertures and the atmospheric phase coherence time.

The maximum usable aperture for an interferometer was derived in chapter II, eq. II.24. Under good seeing conditions (1 arc sec) the maximum efective aperture is 9.5 cm and 32.0 cm for an interferometer without and with high speed star trackers (as explained in II.B.1.b). This corresponds to a total collecting area of 71 cm^2 and 804 cm^2 respectively. Since 804 cm^2 applies to an interferometer with a perfect star tracker, the following calculations will assume a total collecting area of 200 cm^2.

The atmospheric phase coherence time, the period of time

during which atmosphere turbulence will produce less than one radian of phase motion, may be estimated as follows. Since r_o is approximately 10 cm , if we assume a wind of 10 meters per second and apply Taylor's hypothesis, the phase coherence time is r_o/v = 10 msec. This is discussed in greater detail in chapter VI.

The average number of detected photons from a 0.0 mag star can be calculated in the following way. By definition, the flux from a 0.0 mag star (visual magnitude) above the atmosphere is 1030 photons/cm^2/Å/sec at λ=0.55 um. The spectral distribution depends on the temperature of the star's photosphere. For this example a temperature of 6000 °K is assumed. For an interferometer with maximum sensitivity, the spectrum from 0.4 to 0.9 um is divided into 2 colors, one from 0.4 to 0.6 um the other 0.6 to 0.9 um. If we assume the passive optical components, mirrors etc., are perfect, the counting rate for a 0.0 mag star will be eq. IV.12.

$$\text{Counts} = \int_{\lambda_1}^{\lambda_2} K\, B(\lambda)\, QE(\lambda)\, T(\lambda)\, d\lambda \qquad \text{IV.12}$$

$$\text{where} \quad K = \frac{1055 \text{ phot} \times 200 \text{ cm}^2 \times 0.01 \text{ sec}}{B(.55\mu) \qquad \text{cm}^2 \text{ Å sec}}$$

QE is the quantum efficiency of the detector (C31034A)

B is the normalized 6000°K black body spectrum

T is the transmission of the atmosphere

λ_1, λ_2 define the optical bandwidth

Numerical integration of eq. IV.12 yields the count rate of 7.63×10^5 photoelectrons per 10 msec from a 6000 °K star with 0.0

visual magnitude. There is evidence that the quantum efficiency of a typical C31034A tube is significantly lower than stated in the data sheet[65]. If in addition we assume the optics (mirrors etc) have a total efficiency of 0.8, a 0.0 mag star would produce 4.5×10^6 counts per 10 msec.

If the servo requires 250 photons for proper operation (current state of the servo) the magnitude limit would be 8.1 mag. Ultimately, one would expect the servo to be able to operate with 25 photon counts (see V.D). The corresponding magnitude limit is 10.6 mag.

IV.B.2 Accuracy of the Astrometric Interferometer

The accuracy of a ten meter astrometeric interferometer may be calculated as follows. For a 10.6 mag star we expect 25 photon counts per 10 msec. The fringe visibility of an unresolved star due to uncorrelated scintillation would be expected to be 0.85 [25]. The fringe phase error would therefore be 0.37 radians according to eq. IV.11.

The effective wavelength for the long wavelength channel is 0.68 um hence the single color measurement accuracy is $0.68 \times 0.37/(2 \times 10 \text{ meters}) = 8.2 \times 10^{-4}$ arc sec in 10 msec. The two color turbulence corrected position accuracy is therefore $\sqrt{2} \times 50 \times 8.2 \times 10^{-4} = 0.058$ arc sec in 10 msec or 10^{-4} arc sec in 55 minutes. The factor $\sqrt{2}$ arises because measurements at the two colors are subtracted, eq. IV.8, and the factor of 50 is F.

For a 5.6 mag star the photon count is 100 times greater, hence 10^{-4} arc sec could be achieved in 33 sec if the accuracy is limited to photon statistics. Similarly, 10^{-4} arc sec is achievable in 0.33 sec for a 0.6 mag star. For bright stars, the accuracy is limited not by photon statistics but the geometric contribution to the path length discussed previously (IV.A.3).

The error due to the geometric contribution to the path length was estimated in IV.A.3 to be < 0.1 um for 1 arc sec seeing. For a 10 meter interferometer, this corresponds to $2x10^{-5}$ arc sec. However this is a random error which follows atmospheric statistics, hence each 10 msec measurement is not entirely independent of other 10 msec measurements. For bright stars, the astrometric interferometer must average over the same statistics as a conventional astrometric telescope. A conventional telescope must average both refractive and geometric effects while the interferometer only averages geometric effects. In this example the geometric effects are 500 times smaller, $2x10^{3}$ versus 1 arc sec. Following III.C, 10^{-4} arc sec accuracy for the astrometric interferometer is possible with 15 to 30 sec of integration. However, this is only a rough estimate.

In conclusion, the accuracy of the astrometric interferometer is considerably higher than conventional astrometric instruments. In order to take advantage of this improved accuracy, systematic errors must also be minimized.

IV.C Systematic Errors

The astrometric interferometer is radically different from conventional astrometric instruments and therefore the sources of systematic errors for the two types of instrument would not be expected to be similar. Many of the errors of photographic astrometry, see III.B, are related to the use of photographic film, such as magnitude error and emulsion shift. These errors obviously do not exist for the astrometric interferometer. However, the errors of the laser reference interferometer (IV.C.1) are similar to measuring engine errors in conventional astrometry.

While there are few similarities between conventional optical astrometry and the interferometric astrometry, there are many similarities between radio VLBI astrometry and the astrometric interferometer. A number of VLBI errors have no counter part in an optical interferometer. These include errors from unstable clocks, water vapor in the atmosphere, and variations in cable delay. VLBI errors due to antenna offset and antenna flexure have direct counterparts in the astrometric interferometer and will be discussed in IV.C.2.

IV.C.1 Laser Reference Interferometer

In order to achieve 10^{-4} arc sec accuracy, the distance between the central fringes of two stars must be measured to 50 Å precision. This may be accomplished with a laser interferometer.

Since both the laser and stellar interferometers use the same beam splitter, optical delay lines etc. (Fig. V.1),a stellar position measurement is essentially a direct comparison of laser and stellar fringes. The error in the fringe position due to stellar photon noise has been discussed. The laser fringe position error due to laser photon noise is negligible because of the high intensity of laser light.

Several systematic errors in the reference interferometer exist. The laser and stellar beams though using the same optics may be misaligned. A tilt of 3 arc sec would produce an astrometric error of 2×10^{-5} arc sec. Another source of error is the wavelength difference between laser light and star light. A non ideal dielectric beam splitter introduces a phase delay dependent on wavelength. For proper motion and parallax measurements, systematic error result only if the beam splitter is changed or if the star changes color. For absolute position measurements significant errors , 10^{-3} arc sec, may result if the wavelength dependence is not calibrated.

The sources of errors mentioned so far are independent of the size of the field of view. A number of errors, however, are directly proportional to the field of view. The stability of the laser frequency must be better than one part in 3×10^{6} if a field of view of 10 degrees is desired. Changes in atmospheric pressure, temperature, etc., will affect the wavelength of the laser. A two color laser system might be necessary to correct for atmospheric effects on the reference laser system. The correction

would be similar to the two color stellar atmospheric correction system.

IV.C.2 Baseline Coordinates

The distance between central fringes of two stars is proportional to the angle between the stars projected onto the baseline vector. In order to achieve 10^{-4} arc sec accuracy for stars all over the sky, the baseline directions must also be known to 10^{-4} arc sec.

The baseline orientation is to first order, determined by the location of the siderostat mirrors, although as shown in the previous section, internal alignment of the interferometer has a second order effect which may be reduced to 2×10^{-5} arc sec. The location of the siderostat mirrors are in turn dependent on the dimensions of the mirror mounts, bearings, and pedastle.

The basic multiple star switching procedure for simultaneously measuring stellar position and baseline coordinates was discussed in IV.A.2. The requirements of the star switching technique are that irregularities in earth rotation, pedastle motion, etc., are small, 10^{-4} arc sec, over a period of time determined by the switching frequency (10 sec). In addition, the process of switching should not introduce unknown baseline changes larger than 50Å or 10^{-4} arc sec.

The stability of earth rotation at the 10^{-4} arc sec level has not been measured. However it is known that earth rotation is

stable to 10^{-2} arc sec on a time scale of hours to days[66]. It is therefore highly probable that over a 10 sec interval random changes in earth rotation will be much less than 10^{-4} arc sec.

The stability of concrete or other pedestals depends on a number of parameters. However, if the pedestals are shielded from wind and other mechanical disturbances, the major source of instability on a time scale of 10 sec is thermal expansion. For a material with a coeficient of expansion of 10^{-5} /°C (low expansion materials such as invar are 10 to 100 times lower) two one meter tall pedestals must not experience differential temperature changes of more than 0.3 degrees per hour. The use of low expansion materials or thermal insulation may be necessary to maintain stability.

The siderostat mounts cannot be manufactured to 50 Å accuracy at a reasonable cost. However, laser interferometers can be used to measure the position of the siderostat mirrors, relative to mirrors or corner cubes fixed to the pedestal. The stability of the moving mechanical parts is therefore made identical to the stability of the pedestals.

V The One Inch Prototype

This chapter describes the one inch prototype interferometer. The instrument, Fig. V.1 and Fig. V.2, contain three optical subsystems, a PDP 8 computer, and interface electronics. The three optical systems are the fringe tracking servo, angle tracking servo, and laser interferometer. The design philosophy followed throughout the project has been to place the bulk of the complexity of the instrument into computer software rather than in hardware. As a result the design of the software algorithm is much more important than the design of the electronics hardware. The reason for building a servo system in software rather than hardware is that it is much easier to change software than hardware. Long baseline astrometric interferometers have never been built before and it was anticipated that a successful fringe tracking servo would require several trial and error interations.

V.A System Software and Hardware Notation

Before discussing the three optical subsystems, the operating system software will be described. The operating system is a simple multitask system. The software for each of the three subsystems are subprograms that compete for cpu time. The software consists of a large number of tasks each with an assigned priority. The system task scheduler performs the house

INTENTIONAL DUPLICATE EXPOSURE

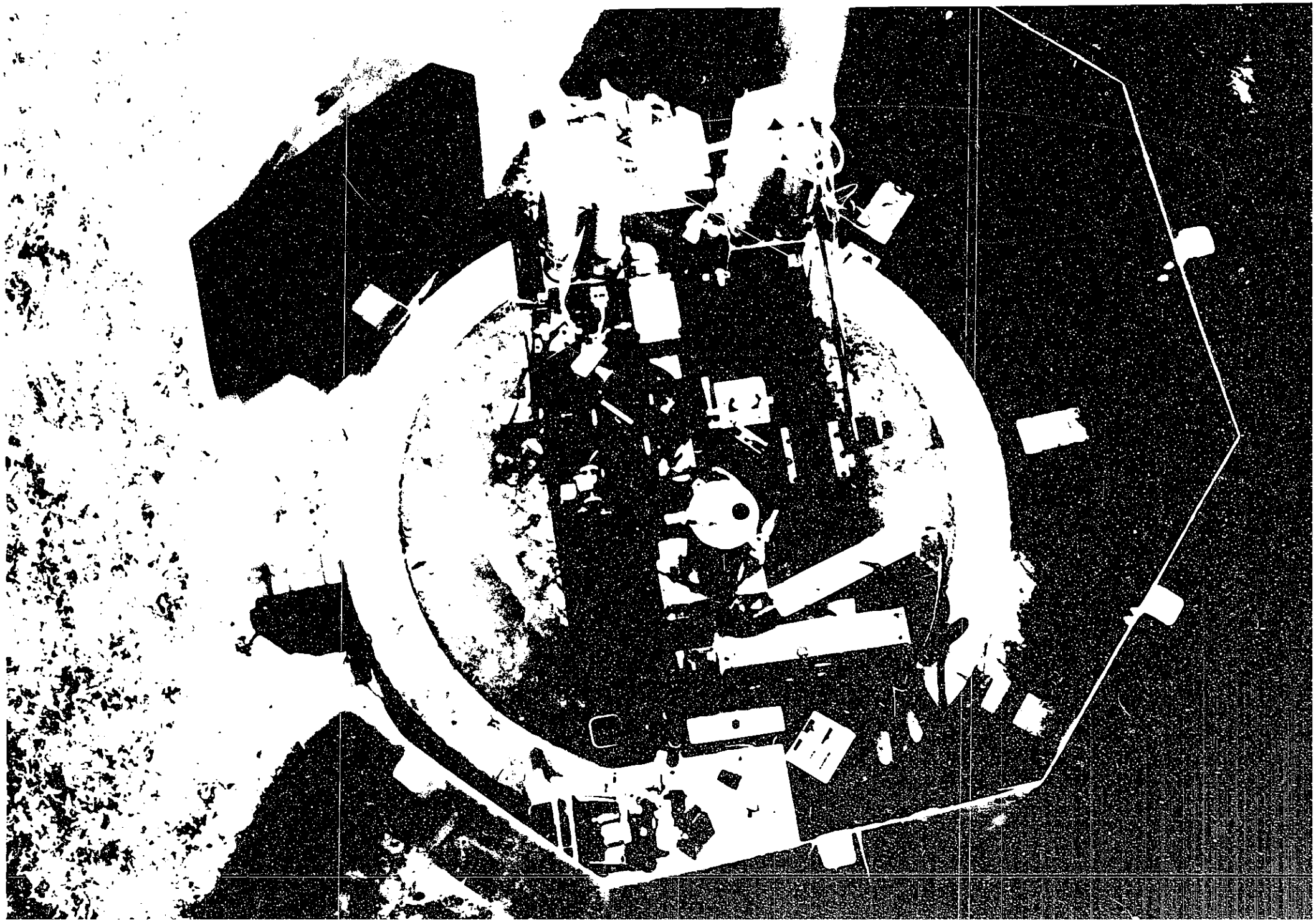

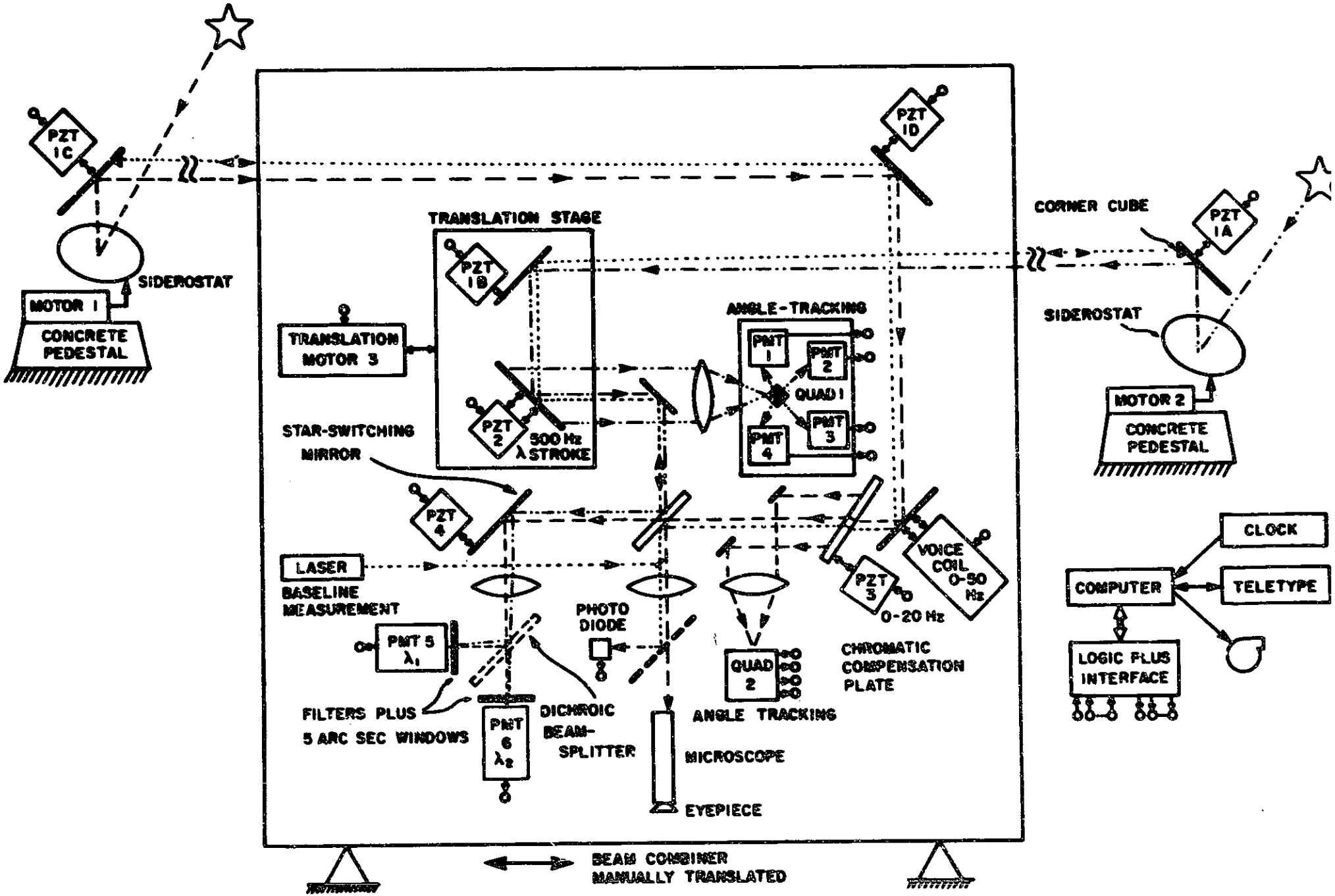
PZT 1C
SIDEROSTAT
MOTOR 1
CONCRETE PEDESTAL
PZT 1D
TRANSLATION STAGE
PZT 1B
TRANSLATION MOTOR 3
PZT 2
500 Hz λ STROKE
ANGLE-TRACKING
PMT 1
PMT 2
QUAD 1
PMT 3
PMT 4
STAR-SWITCHING MIRROR
PZT 4
LASER
BASELINE MEASUREMENT
PMT 5 λ1
PHOTO DIODE
FILTERS PLUS 5 ARC SEC WINDOWS
PMT 6 λ2
DICHROIC BEAM-SPLITTER
MICROSCOPE
EYEPIECE
QUAD 2
ANGLE TRACKING
PZT 3
VOICE COIL 0-50 Hz
0-20 Hz
CHROMATIC COMPENSATION PLATE
BEAM COMBINER MANUALLY TRANSLATED
CORNER CUBE
PZT 1A
SIDEROSTAT
MOTOR 2
CONCRETE PEDESTAL
CLOCK
COMPUTER
TELETYPE
LOGIC PLUS INTERFACE

keeping chores of saving the machine state for an interrupted task, giving control to a higher priority task, and restarting the interrupted task when the higher priority task is through.

A task may be in one of three states. A task is in the executing state if it currently has control of the cpu. A task is in the active state if it is waiting for control of the cpu. A task is inactive if it does not have control and is not waiting to get control. Some tasks are activated periodically by the system clock. Others are activated by commands typed into the teletype keyboard. Last of all, tasks may be activated by pushing a button on a "paddle" that is interfaced to the computer.

Under normal conditions aproximately 85% of the cpu time is used. The laser interferometer task uses aproximately 20% of the time. The angle tracker tasks use 15% of the time, the fringe tracking servo task uses 30% of the time and 20% of the time is used by the system. Several earlier versions of the software were unreliable because occasionally the tasks and system overhead required more than 100% of the available cpu time.

When a task requires input data, it is assumed that the data has been made available by another task or that the data is available from an input device. On output, direct output is usually performed on the high speed devices such as the pzt (piezoelectric transducer), voice coil and LED's and buffered output is performed on the low speed devices such as the teletype and stepper motors. In buffered output, the data is stored in a buffer in core and a very low priority task is enabled. This low

priority task, which will receive control of the cpu only when higher priority tasks have relinquished control, actually performs the output operations using the data in the buffer.

When interpreting flowcharts, each task can be viewed as an independent program. However, sometimes it is necessary to know the order in which several quasi-independent tasks are executed. Explicit scheduing commands are sometimes given by one task to enable or kill another task. When several tasks are simultaneously enabled, their priorities determine the order in which they are executed. In some cases, the order of execution is important because a high priority task generates the data for a lower priority task. Therefore, in addition to conventional flowchart symbols, each task contains a description of its priority and a description of how often and by whom it's enabled or killed.

The schematic diagrams for the electronics hardware are almost always block diagrams. In most cases, the procedure for filling in the details is straight forward. The main reason for only supplying block diagrams is that most of the electronics hareware are computer interfaces for what is effectively an obsolete computer. Significant differences in the I/O bus structure between the PDP-8 and PDP-8/A (current model in the PDP-8 series) exist. In addition many of the blocks in the block diagrams will soon be integrated into single integrated circuits as micro and minicomputer interfacing is made simpler by integrated circuit manufacturers.

V.B Laser Interferometer Subsystem

Ideally, the laser system should be used to produce a mechanical system immune to distortion from mechanical vibration, mechanical flexure, and temperature variations. In the prototype however, the laser interferometer only measures the position of the mirrors.

The laser interferometer is a Michelson interferometer which uses much of the optics used by the stellar interferometer. In this way, motion of the mirrors on the baseplate will be monitored by the laser interferometer. Fig. V.2 shows that the path of laser light is very similar to the path of the star light inside the interferometer. Fig. V.3 illustrates the relation between the position of the stellar beam and laser beam at the beam splitter. In addition, the two beams are tilted with respect to each other so that the returning laser light will not enter the stellar fringe detection phototube.

Laser light is detected by the photodiode, mounted on a separate plate as shown in Fig. V.1. The laser interferometer electronics and software was built by D. McDonough as a senior thesis (June 1976 EE&CS). The pathlength in one arm of the laser interferometer is modulated by a piezoelectrically driven mirror (Fig. V.1 and V.2). The photodiode output is amplified and then converted into digital format for input into the computer. The software samples four outputs from the analog to digital

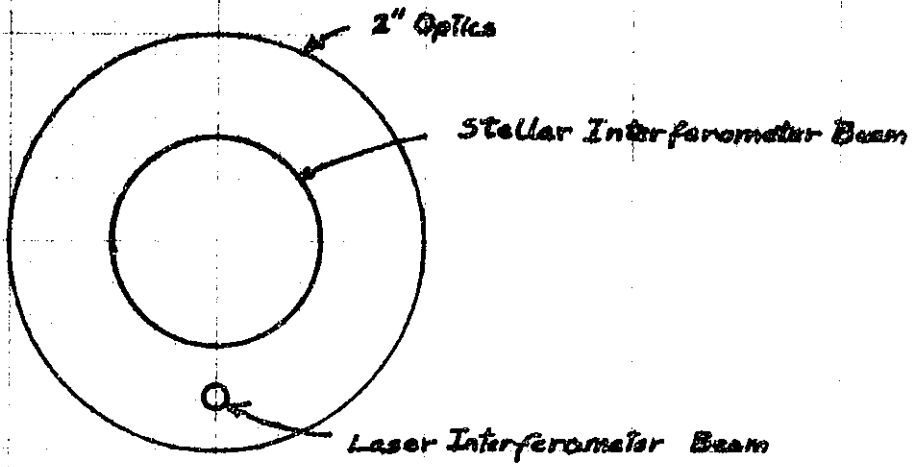

FIG. V.3 Relative Positions of Stellar and Laser Interferometers

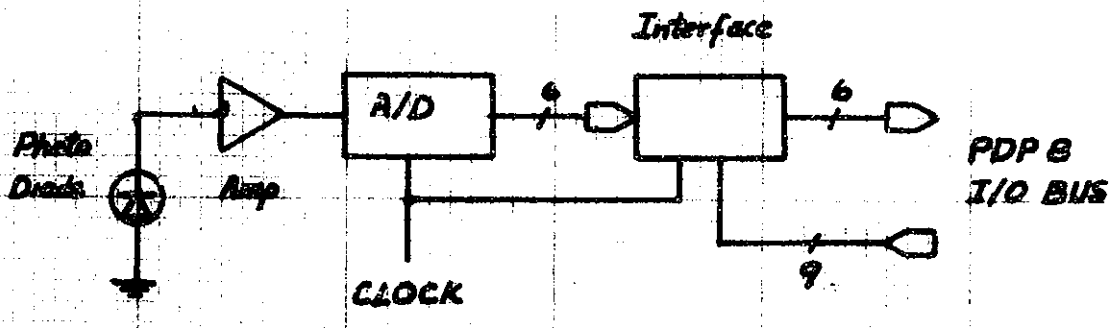

Electronics for Laser Interferometer

FIG. V.4

converter per modulation cycle and calculates a fringe position with a demodulation algorithm similar to the algorithm used to determine stellar fringe position (to be described later). Fig. V.4 is a schematic of the electronics for the laser interferometer and Fig. V.5 is a flowchart of the laser interferometer software.

Several additions to the laser system should be made for an astrometric instrument. The first is that the position of the siderostat mirrors should be monitored by interferometers. During operation, the interferometer will measure the relative fringe positions of several stars by switching between the stars. Since the siderostat mirrors must move to each of the different stars, the baseline vector will change as the mirrors tilt, unless the mirrors rotate on perfect bearings (to 0.01 λ). Since mechanical bearings of this high level of accuracy are extermely difficult to manufacture, the baseline vector which is determined by the postion of the siderostat mirrors must be monitored with a laser interferometer system.

The second modification is that the laser fringe position be used to compensate for vibration, thermal expansion and other sources of mechanical instability. Fig. V.6 illustrates how such a system might operate. Such a system could have been implimented on the one inch prototype if the memory and speed of the computer were significantly greater.

V.C Star Tracker Subsystem

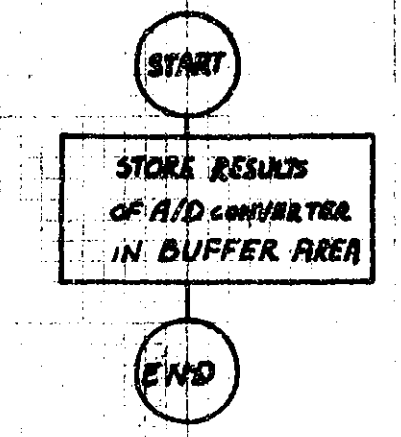

Interupt Handler Entered via hardware interupt every 500 μ sec.

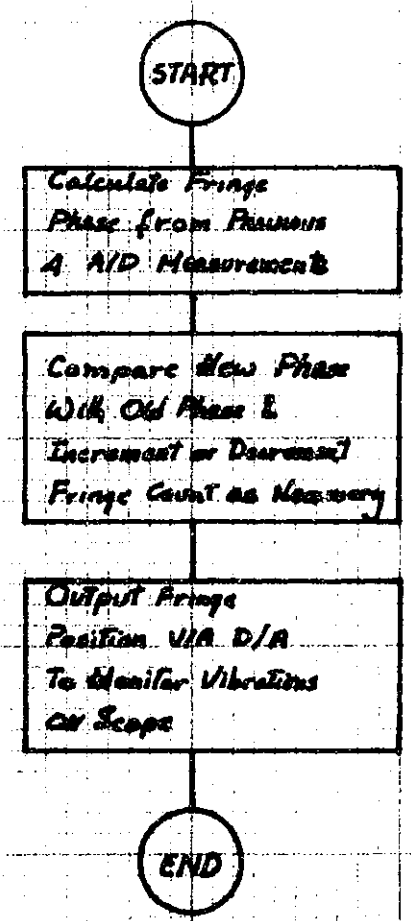

Laser Interferometer Task Scheduled every 2 msec.

FIG. V.5 Laser Interferometer Software

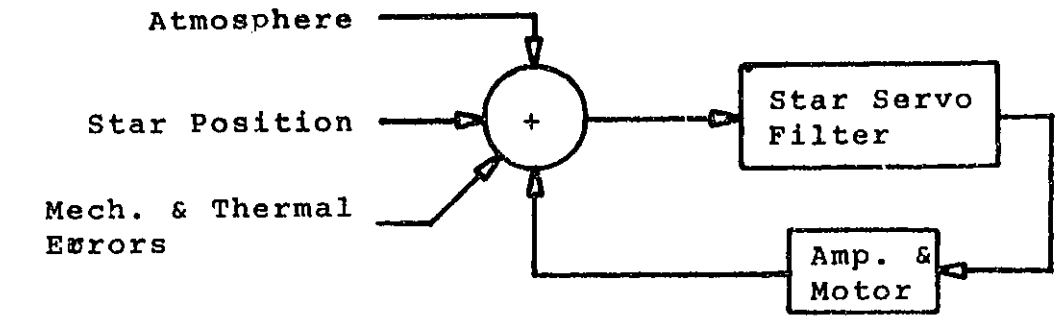

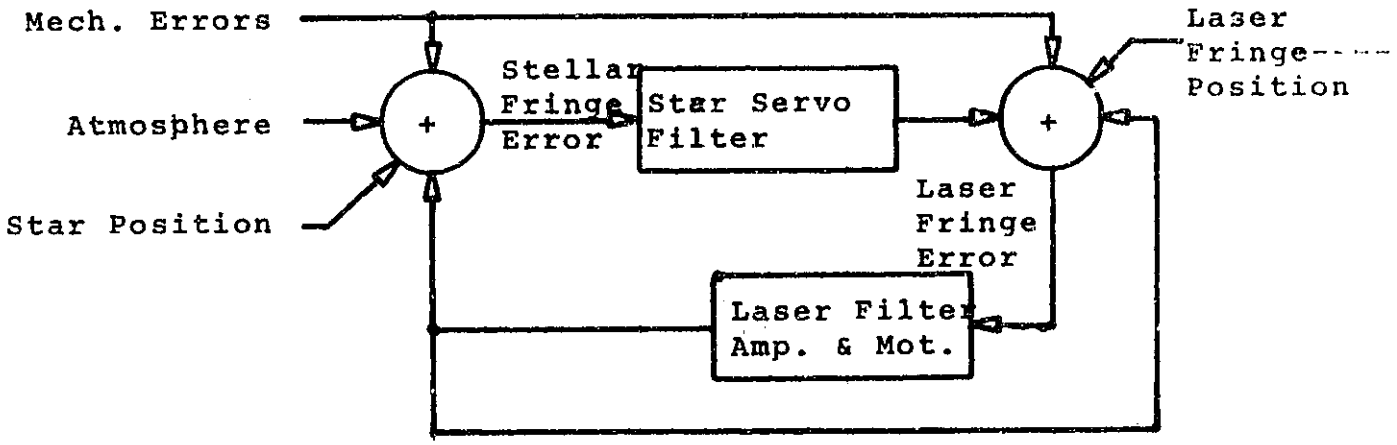

FIG. V.6 Modified Stellar/Laser Fringe Tracking Servo

Two angle tracking servos are used in the one inch prototype to keep the interfering wavefronts parallel. In addition, the error signal from the angle tracking servo is used as described in chap 6 to calculate various atmospheric parameters. The servo was not designed to track the fast image motion due to atmospheric turbulence, only the motion due to earth rotation. Even for tracking earth rotation, a closed loop system was necessary. The two independent siderostats must track the star with an error less than 4 arc sec over a period of several hours. While telescope drives with this level of accuracy exist, the cost of a closed loop tracker is much less than the cost of an open loop system at this level of accuracy. An additional advantage of using star trackers is that the telescope drives need not be precisely aligned with the north pole.

Since both east and west star trackers operate in the same way, I will explain only the operation of one of the star trackers. Fig. V.7 is an optical schematic of the west star tracker. Light from the star is directed by the siderostat mirrors toward the annular mirror. The inner one inch of the beam goes through the hole in the annular mirror and is used by the stellar interferometer. The rest of the light is used by the star tracker. The lens, mirrors and microscope objective form an image of the star on the four quadrant detector. The effective focal length of the star tracker telescope is approximately 5 meters.

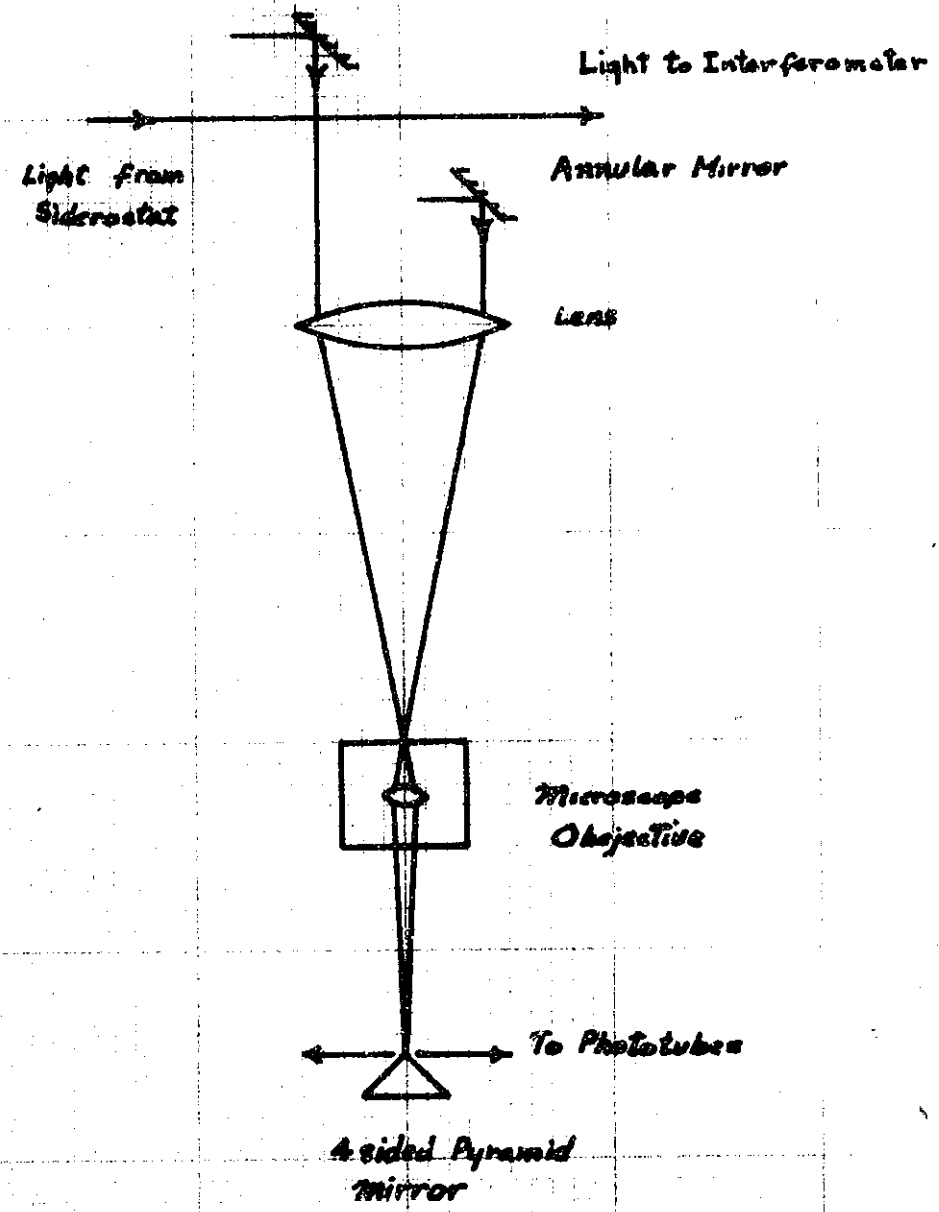

Fig. V.7

Optical Schematic of Star Trackers

The quadrant detector consists of a four sided pyramid mirror and four phototubes operated in the photon counting mode. The two quadrant detectors may be recognized in Fig. V.1 as the cluster of four phototube assemblies. The phototube assemblies (round cylindrical objects in cluster of four in Fig. V.1) each contain a high voltage supply, preamplifier, discriminator and pulse shaper. Originally, twelve such assemblies were built by P. Kababian about 7 years ago for a stellar diameter interferometer. The use of these phototubes resulted in a very significant reduction in the cost of the project.

The image of the star is focused on the tip of the four sided pyramid and the light is reflected into the four corresponding phototubes. The error signal is derived from the counting rate of the four tubes, A, B, C, and D, by equation V.1 and V.2.

$$E_{rr}\ (A_Z) = \frac{A+D-B-C}{A+B+C+N} \qquad V.1$$

$$E_{rr}\ (E_L) = \frac{A+B+C-D}{A+B+C+D} \qquad V.2$$

The four quadrant detector is approximately four times as sensitive as a star tracker using an image disector tube and twice as sensitive as a knife edge type error sensor. The choice of the quadrant detector was however based on mechanical complexity and cost considerations since almost any error sensor will work for a servo designed to track the motion of Polaris.

The phototubes are interfaced to the computer as illustrated

in Fig. V.8. Every clock cycle the contents of the counter are stored in a latch, the counter reset, and an interupt request generated. The clock frequency may be changed in software. An interupt service routine then reads the number of photons detected in the provious cycle and resets the interupt request line.

The siderostat mirror mount is simply a conventional gimbal mounted mirror with stepper motors attached to the micrometer knobs. Anti-backlash gears were used to reduce the size of the step to 4 arc sec of tilt per step. For fine motion control piezoelectric ceramic transducers were used in series with the micrometer drive. The piezoelectric transducers were controlled by the computer through an eight bit D/A converter and a high voltage amplifier. This gave a minimum step size of 0.08 arc sec.

Despite the fact that the whole gear train was spring loaded, there were several arc sec of backlash in all the stepper motor drives. The exact amount of backlash varied with time, temperature, position, and from motor to motor. The backlash of the piezoelectric elements was much less than an arc sec (not measureable). On the other hand, there were significant nonlinearities (0.5 arc sec) in the piezoelectric transducers. The defects described in this paragraph would prevent proper operation of the interferometer if the star trackers were operated open loop. For closed loop operation, these errors are reduced by a factor proportional to the servo loop gain. The

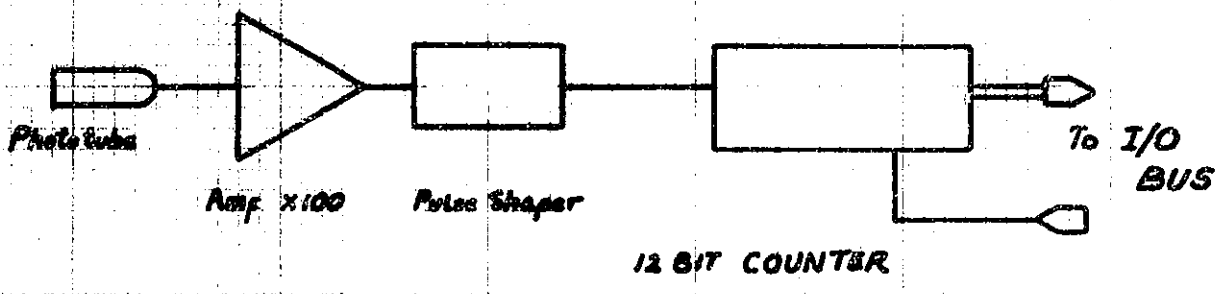

Fig. V.8 Photo tube Electronics

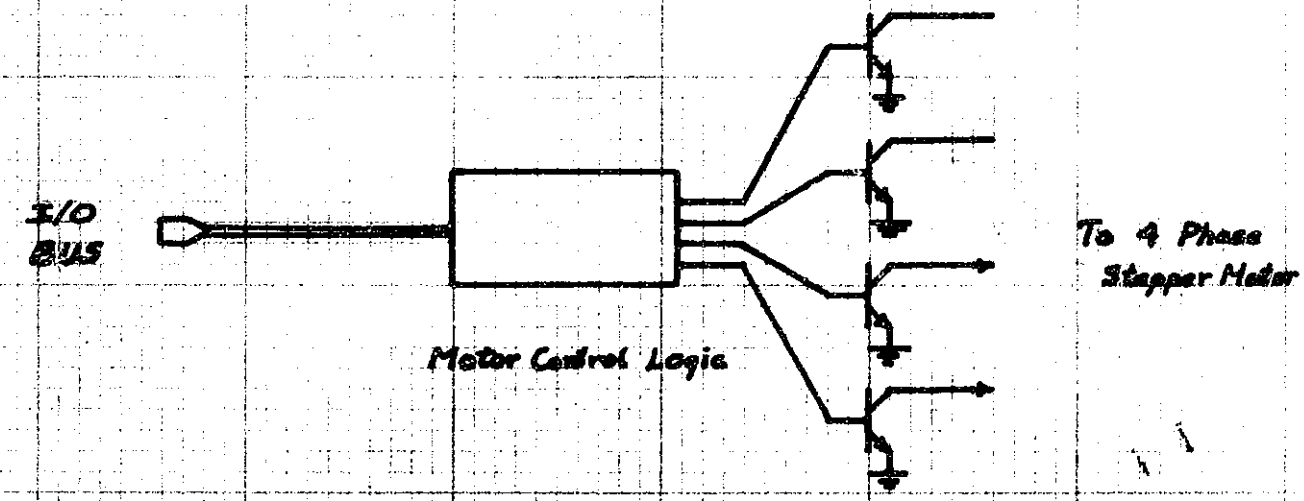

Fig. V.9 Motor Electronics

motor control electronics are shown in Fig. V.9.

The star tracker software is illustrated in Fig. V.10. The sidereal drive software was a subroutine which calculated the stepper motor positions at the current sidereal time. Since no effort was made to calibrate the errors in the gear train, the sidereal drive was only used to position the siderostats to within the field of view of the star trackers (2 arc min).

The angle tracker servo task operates as follows. The clock is set with a 20msec period. As a result, every 20 msec the computer read in the number of photons detected in the previous 20 msec. The photon counts A, B, C, and D are corrected for individual differences in quantum effiency, dark count and background light level. Another task not shown in Fig. V.10 can be made active from the keyboard to measure the background light level. In future instruments it should by possible to have the computer actuate shutters to individually calibrate the phototubes.

If the servo is enabled, the software checks if a star is in the field of view by comparing the total number of photons detected in the previous 20 msec to a predetermined threshold. If Polaris is in the field of view, the manual stepper motor controls are disabled and the servo loop closed. If no star is in the field of view, the loop is left open, this prevents the computer from "tracking noise" when a cloud drifts overhead.

When the loop is closed, the software calculates the azimuth and elevation error using eq. V.1 and V.2. The sidereal drive

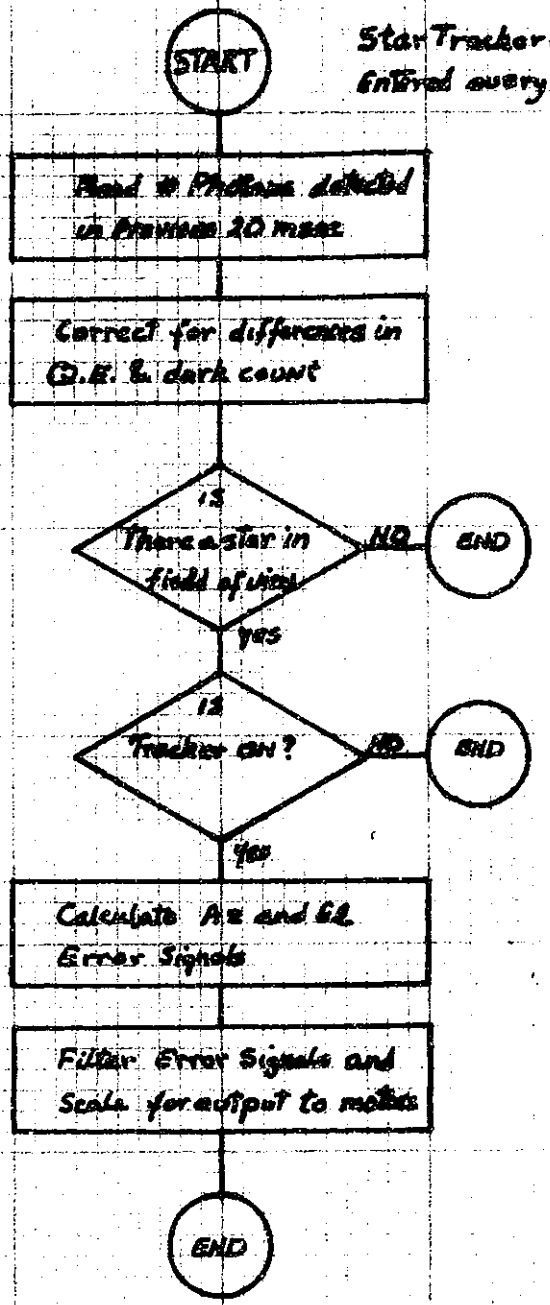

FIG. V.10 STAR TRACKER SOFTWARE

task is also killed if it is active. The motors are advanced an amount proportional to the error signal. Usually this only involves changing the voltage to the piezoelectric transducer, but if the pzt reaches the end of its travel, the stepper motor is stepped and the pzt moved back so that the total effective motion is what was desired. Typical errors during this operation is less than 0.3 arc sec when the stepper motor is not reversing direction.

The current values of A, B, etc. represent the average photon flux over the previous 20 msec. The derived position is therefore the most probable position in the middle of the 20msec period or 10msec before the start of the computation cycle.

Since the task is made active every 20 msec, a constant error signal will result in a constant motor velocity. The servo may then be described by the difference equation V.3.

$$\frac{\Delta M}{\Delta t} = \frac{m_{i+1} - m_i}{\Delta t} = k E_i \qquad \text{V.3}$$

S_i = star position at time i

m_i = motor " " " "

$E_i = S_i - m_i$ error signal

For $t \to 0$ the difference equation becomes the differential equation eq. V.4.

$$\frac{dE}{dt} - k'E = \frac{dS}{dt} \qquad V.4$$

E = error signal

S = stellar position

This is perhaps the simplest possible servo. Since the servo was designed to track the rotation of the earth at 10^{-5} Hz the errors in the gear train become insignificant. The servo time constant was 4 sec, much too slow to track the fluctuations due to atmospheric turbulence. The rms tracking error was therefore determined by atmospheric seeing. This varied between 2.5 and 4.5 arc sec (5 to 9 arc sec seeing) at Wallace Observatory.

While this servo could be used to track the fast fluctuations caused by turbulence, it would be desirable in the future to use a filter matched to the angle of arrival spectrum to achieve a minimum error.

V.D. Fringe Tracking Servo

V.D.1 Introduction

The fringe tracking servo consists of three parts. The first is a device to measure fringe phase or position. The second is a variable optical delay line. The last is a control system which uses the information from the phase measurement to control the delay line.

V.D.2 Phase Measurement

There are many ways to measure fringe phase. Before describing the system used in the one inch prototype, I will briefly describe a few of the alternatives.

A fringe is a sinusoidal variation in the intensity of light at the output of the interferometer as expressed in eq. V.5 for monochromatic light.

$$I = I_o(A\cos\phi + 1) \qquad V.5$$

$\phi = \tau 2\pi/\lambda$

A= fringe amplitude $0<A<1$

I_o =Intensity of starlight

All current methods determine fringe phase by varying ϕ or τ by a known amount while measuring the intensity of light at the output of the interfermeter. Since the expression for I in eq. V.5 is a function of three unknowns, a minimum of three independent measurements are necessary.

If a dielectric beam splitter is used to combine the interfering wavefronts, the two outputs are 180° out of phase and in theory only one additional measurement is necessary for unambiguious determination of phase. One technique for introducing a controlled variation of path length or phase is to use piezoelectric transducer or acoustic optic phase shifter. The phase or pathlength is varied periodically and the output of the

nterferometer is synchronously demodulated to obtain the fringe hase. Another method is to use polarization multiplexing instead f time multiplexing. A quarter wave plate is inserted into one rm of the interferometer. The relative pathlengths of the two rthgonal polarizations will differ by 1/4 wave. At the output of he interferometer the two polarization states are separated by a olarizing beam splitter.

In place of a dielectric beam splitter, a diffracting beam plitter may be used. Kabebian [4] gives an excellent description f the operation of this type of interferometer. Again two utputs 180° out of phase are available and fringe phase measure ill require a third measurement using temporal or polarization ncoding as described in the previous paragraph.

A piezoelectric pathlength modulator was chosen for the one nch prototype because of its simplicity. The modulation is a riangle wave at 500 Hz, fig V.11. The resulting signal from the etector at the output of the interferometer is also shown in ig. V.11. The output is digitized, fig V.11, and synchronously emodulated to produce fringe phase. Each cycle, 2 msec, is ivided into four parts. The photon counts during these intervals , B, C, and D are used to calculate the fringe phase using eq. .6.

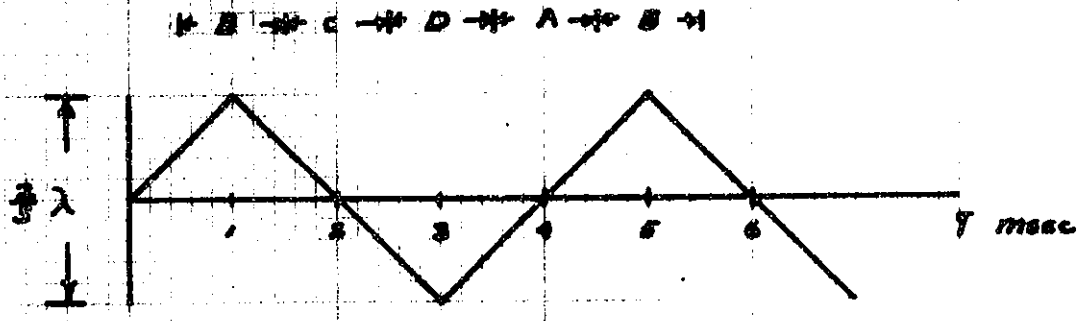

Triangle modulation waveform

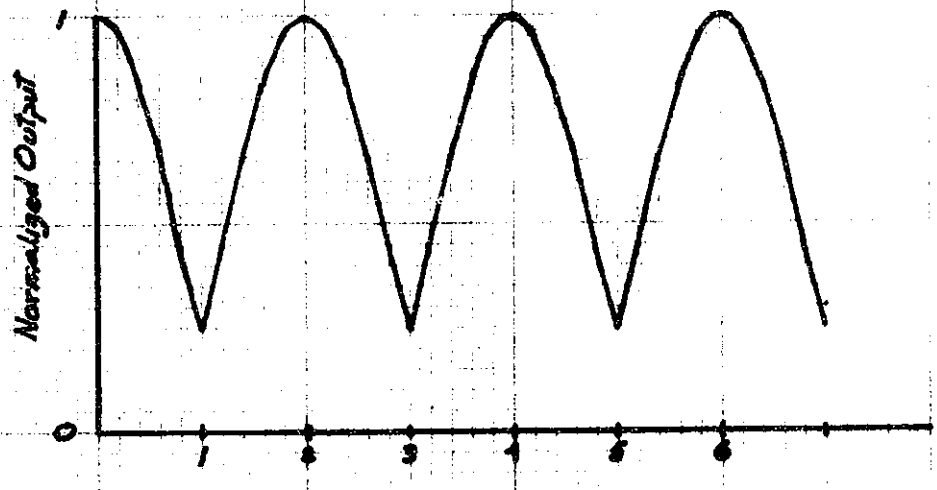

Modulated Phototube Output

FIG. V.11 Fringe Deflector Modulation Waveforms

$$\phi = \text{TAN}^{-1}\left[\left(\frac{B-D}{A-B+C-D}\right)\sqrt{\frac{3}{4}}\right] \qquad \text{V.6}$$

This modulation scheme is slightly less sensitive than the one described in chapter 4.

The hardware for the fringe detector is illustrated in fig. V.1. The phototube detects photons via the photoelectric effect. The electron multiplier provides a gain of approximately 10^5. The signal is further amplified by the preamp (gain =100). The preamp is connected to a discriminator which is set to reject pulses with an amplitude less than 0.25 of the average single photoelectron pulse. The pulses are then counted in the computer interface.

The system clock at 4 MHz is counted down to 2 KHz. Two indentical sets of counters are used to produce two 2KHz outputs whose relative phase can be controled by the computer software. One of the 2 KHz signals is used to generate a 500 Hz triangle wave which is amplified by a high voltage amplifier to drive the piezoelectric transducer. The other 2 KHz signal is used to reset the counters in the computer interface and generate an interupt.

The photon counts A, B, C, D, are read into the computer by the interupt handler. Every 10 msec ,20 samples, the fringe phase is calculated using eq. V.6.

V.D.3 Delay Line

The delay line as shown in fig. V.1 is a mirror mounted on a parallelogram type flexure bearing driven by a voice coil. The mechanical resonance of the bearing is approximately at 50 Hz. The mechanical Q is approximately 10. Below 5 Hz, the position of the mirror is linearly proportional to the current going through the voice coil. Since a flexure bearing has no backlash, the resolution of the delay line is determined by the resolution of the digital to analog converter and the gain of the power amplifier. The gain of the amplifier was set so that the least significant bit of the D/A was 1/16 of a wavelength. For economic reasons a 12 bit D/A was used and hence the range of the delay line was 256 λ or 0.13 mm.

In addition to the voice coil operated delay, a delay line using two mirrors mounted on a translation stage driven by a motor is used for coarse positioning.

In the next version of this instrument, the piezoelectric transducer will be used as a delay line as well as a modulator. The total delay will then be the sum of the three delay elements. Table V.1 shows the range resolution and frequency response of the various delay lines.

	Range	resolution	freq. res.
PZT	0.5 λ	0.001 λ	200Hz
Voice coil	256. λ	0.062 λ	5Hz
T stage	$2 \times 10^6 \lambda$	0.5 λ	0.5 Hz

V.D.4 Control Algorithm

V.D.4.a Introduction

In a long baseline interferometer, atmospheric and instrumental pathlength errors will be much larger than the coherence length of a broad band source (2 wavelengths). Hence it is necessary to search for the fringe by moving the delay line.

After the search algorithm finds a fringe the servo is turned on to track the fringe. At high light levels, the first fringe found may not be the central fringe. As a result, a wobble algorithm must be used to find the central fringe. The wobble algorithm introduces an offset into the fringe tracking servo to force a different part of the fringe to be tracked. The fringe visibility at different offsets are compared to determine if the fringe that is being tracked is the central fringe.

At low light levels, near the threshold of operation, the servo will occasionally lose track of the fringe. Since the fringe is known to be nearby, the fringe recovery algorithm will take advantage of this fact to find the fringe. The threshold of operation can be defined as the point where the amount of time spent in the fringe recovery phase is equal to the time spent in the fringe tracking phase.

The algorithms described have been implimented in software. In most cases, the implimentation is straight forward. Two

algorithms will be discussed in greater detail. One is the fringe amplitude signal-to-noise ratio monitor. The second is the servo algorithm.

V.D.4.b Fringe Amplitude Monitor

It was explained in the previous section that the presence or absence of fringes was determined by the fringe signal-to-noise ratio. In the prototype interferometer, this signal-to-noise ratio (FASN) was estimated by eq. V.7 (see Appendix 3).

$$FASN = \frac{(B-D)^2 + [(A-B+C-D)1.15]^2}{N} \qquad V.7$$

FASN is calculated every 10 msec. Unfortunately, the estimate of FASN, eq. V.7 from 10 msec of data is a very noisy estimate. Fig V.12 are histograms which show the distributions of FASN due to photon statistics when fringes are present and when they are absent. The data was obtained with a laser as a light source, the interferometer was deliberately misaligned to obtain the probability distribution of FASN when fringes were absent.

Because of the high noise level for FASN the presence of fringes cannot be determined from just 10 msec of data except, for bright stars. When the instrument is searching for a fringe each 10 msec determination of FASN is compared to a predefined

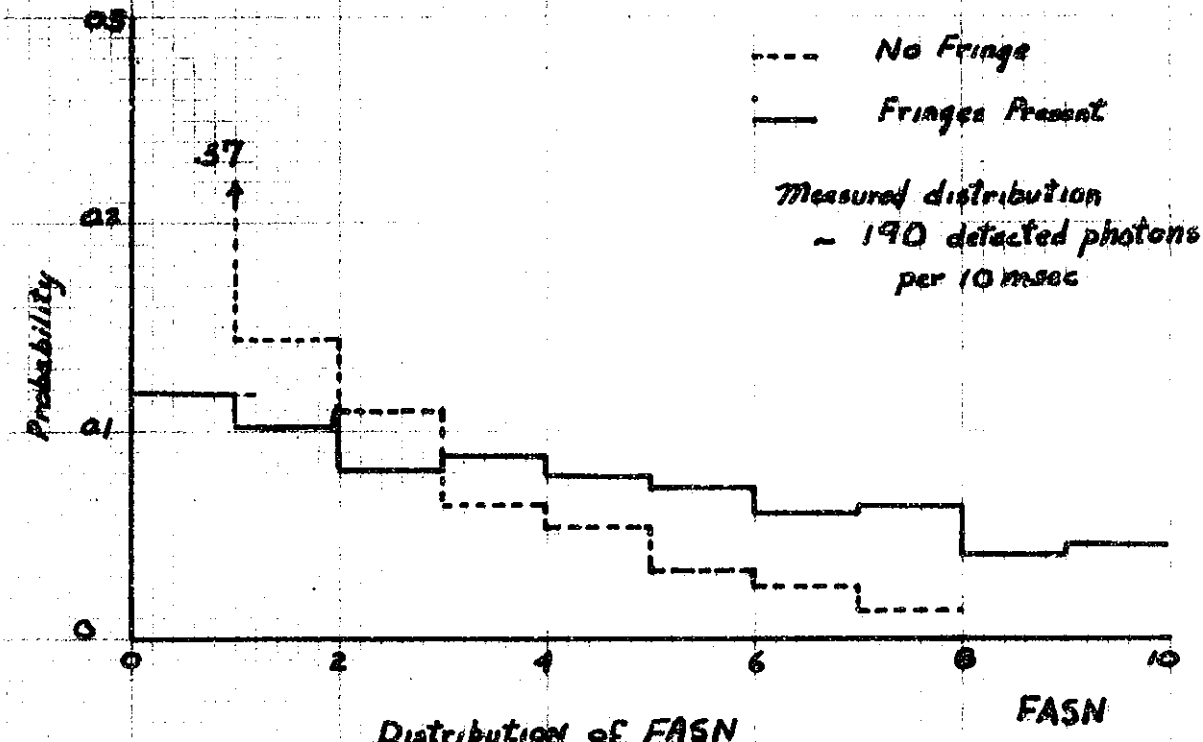

Distribution of FASN

Fig. V.12 Histogram of FASN

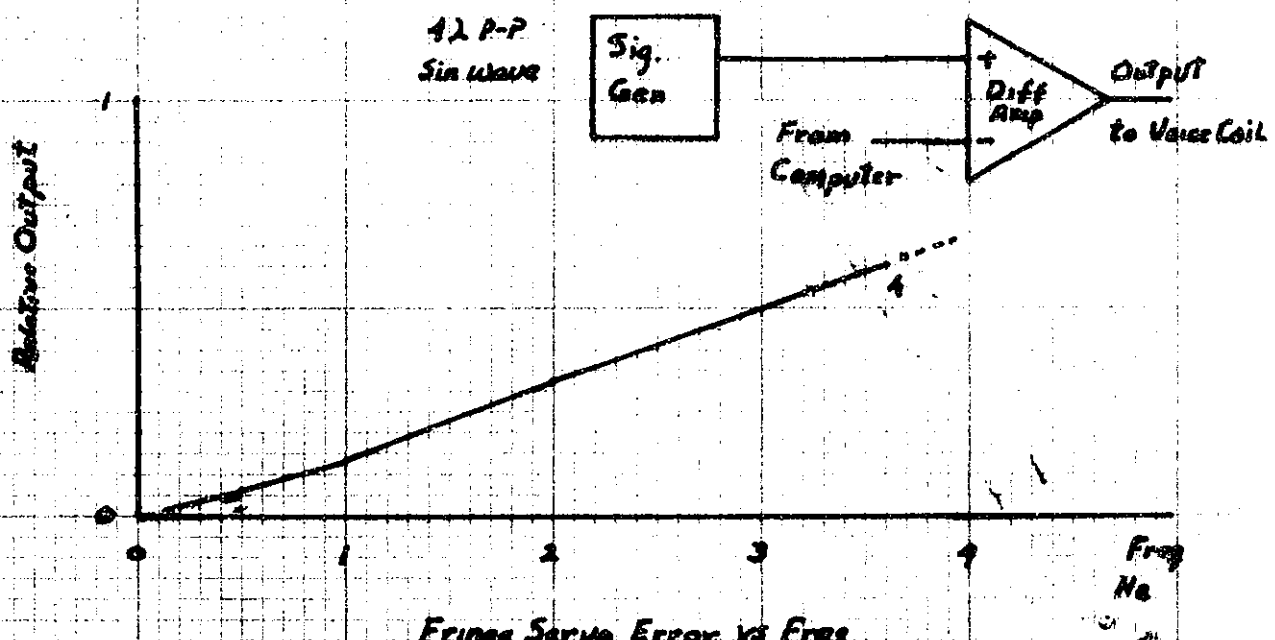

Fringe Servo Error vs Freq

Fig. V.13 Fringe Tracking Servo at High Light Level

threshold. If FASN is below the threshold, the search would continue. If FASN is above the threshold, the servo would be turned on. The system is now in the semilock mode. If the value of FASN for subsequent 10 msec intervals is less than the threshold the search mode is reinstated. If however, FASN is above the threshold for N successive 10 msec intervals the system enters the lock mode (N=8 in the present sytem).

The lock mode differs from the semilock mode in that a single 10 msec drop, FASN below the threshold, will not turn off the servo in the lock mode. In the one inch prototype FASN must be lower than the threshold for 30 msec before the servo is turned off and the search mode reinstated.

The purpose of the fringe amplitude signal to noise monitor is to determine if the phase calculated by the fringe phase subroutine is meaningful. Two modes of operation are necessary. The control algorithm can respond quickly with the semilock mode if a fringe is encountered. On the other hand, the lock mode is much more stable because several 10 msec intervals of data are used to determine if the system should enter or leave the lock mode.

Numerous variations this fringe amplitude monitor system are possible. The particular algorithm used for the one inch prototype was simply the first one that worked in the lab at a light level of 200 photoelectrons per 10msec(the measured flux at Wallace was aproximately 260 photoelectrons/10msec). Operation at 200p/10msec was marginal, as much time spent in the fringe

recovery mode discussed earlier as in the tracking mode.

The fringe amplitude monitor will be a key part of any long baseline interferometer where the fringe must be found, and the design of future interferometers should include a systematic study of a number of different fringe monitor algorithms. Currently, the fringe amplitude monitor algorithm requires almost twice as much cpu time as the servo algorithm and is a significant drain on the computational resources of the computer.

V.D.4.c Servo Algorithm

As mentioned previously, temporal coherence is maintained even if path length differences are 2λ. As a result, a very simple servo may be used. The servo algorithm consists of three parts. The first part calculates the fringe phase from the photon counts. The second part generates a linear error signal from the fringe phase information. The third part filters the linear error signal and outputs the result to the voice coil delay line.

The calculation of fringe phase was described earlier and will not be repeated. The fringe phase would a suitable error signal for the servo if fringe motion was always less than $\lambda/2$. However, the 2π periodicity of fringe phase would cause erratic servo behavior if the servo error was ever greater than $\lambda/2$. In the one-inch prototype,the fringe count was added to the fringe

phase to produce a linear error signal when the error was greater than $\lambda/2$.

The third and last part of the servo algorithm is the error signal filter. For the one inch prototype, the output was simply the integral of the error signal as expressed by eq. V.9.

$$\text{Output Voltage} = k \int_{t_0}^{t} \text{Error}(t)\, dt \qquad \text{V.9}$$

k is the loop gain

t_o is the time at which the servo was turned on

This very simple algorithm is sufficient because it is not necessary to track the fringe with high accuracy. For astrometry, it is only necessary to measure the fringe position accurately. Therefore it is also not necessary for the servo response time to be less than the atmospheric coherence time as in many other active optical systems. The major difference between this active system and others is that the accuracy of the measurement is not directly dependent on the accuracy of the servo.

Two sets of measurements were made of the performance of the fringe detector. The first set measured the performance of eq. V.9 for tracking fringes. The second set measured the performance of the fringe finding algorithm.

The first test was conducted at a high light level, 600 photons/10 msec with an attenuated laser beam. A differential amplifier was placed between the computer and the power amplifier for the voice coil delay line. A signal generator was connected

to produce a 4 λ peak to peak sine wave on the delay line. The servo loop was closed with a command to the computer. Fig. V.13 is a plot of the output of the diff. amp. divided by the output of the signal generator versus frequency. The servo was unstable at 4 Hz. It would occasionally jump from one fringe to the next. At 4 Hz the servo must track fringe motion at ~50λ/sec.

The fringe finder was tested with a white light point source (@ 3200°K). The algorithm described previously found fringes at 200 photons/10msec. The quantities A, B, C, and D, were monitored with a D/A converter and a scope. Fig V.14 is a photograph of the scope display which shows the presence of fringes as well as the presence of a great deal of noise. (Note that A,B,C,D are offset from their definition in section V.D.2. The value A is not known until the beginning of interval B.)

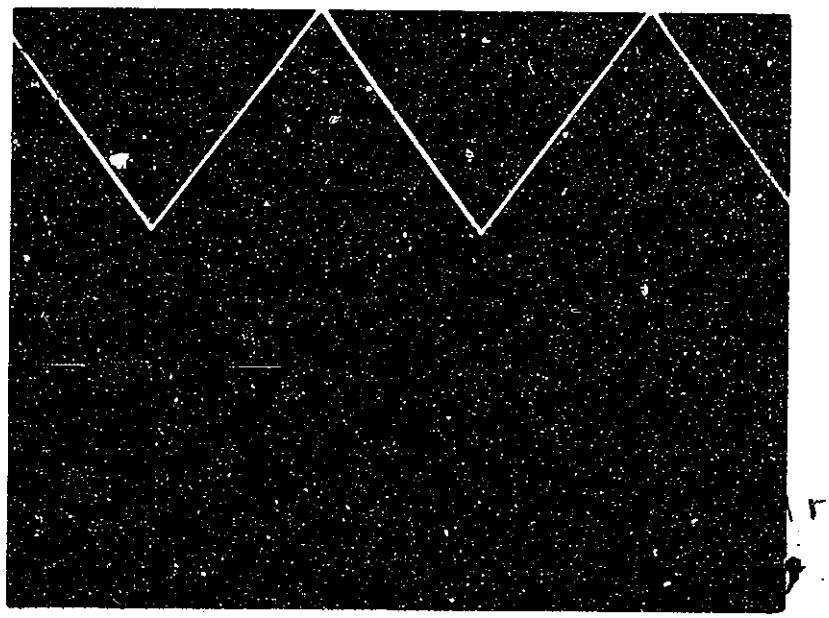

Fig. V.14

[illegible] λ [illegible] the [illegible] line. The servo loop was closed with a connection to the computer. Fig. V.14 is a plot of the output of the [illegible] divided by the output of the signal generator versus frequency. The servo was set to 6 Hz. It would occasionally jump from one fringe to the next. At 6 Hz the servo must track fringe motion at λ/sec.

The fringe finder was tested with a white light point source at [illegible] $^{\circ}$K. An electronic interface was built to [illegible] photomultipliers. The quantities α, β, γ, and δ, were monitored with an A/D converter and a scope. Fig. V.15 is a photograph of the scope display which shows the presence of fringes. With the presence of a great deal of noise. These signals, of course, arise from their definition in section V.[illegible]. The value Δ is also seen, with the beginning of interval [illegible].

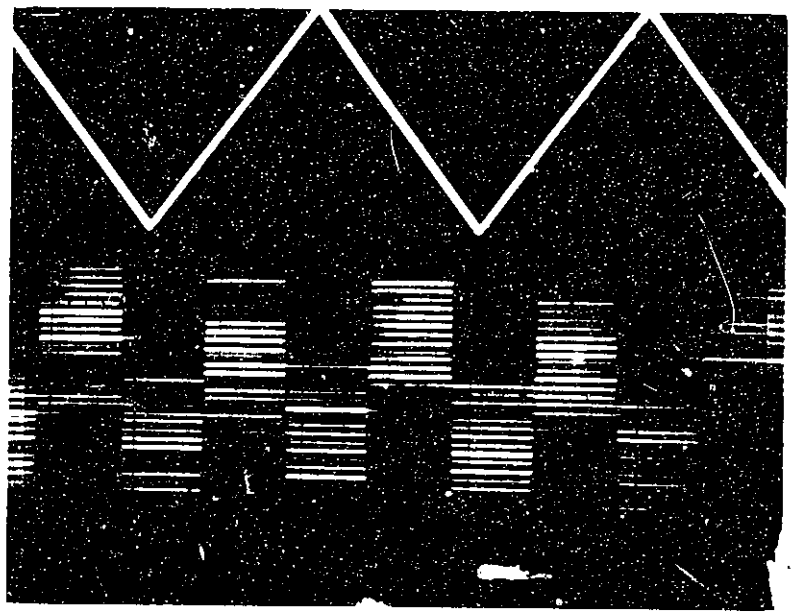

Fig. V 14

VI Measurement of Atmospheric Parameters

VI.A Introduction

The original goal of the one inch prototype interferometer was to track stellar fringes at Wallace Observatory. After numerous unsucessful tries, the atmospheric turbulence data was recorded and analysed to determine the values r_o and τ_o . These two quantities, determine the maximum usable aperture and integration time for a servocontrolled interferometer. In addition, the data was used to determine the effects of seeing on the noise in conventional astrometric instruments.

All of the atmospheric measurements were derived from the star tracker error signals. The star tracker quadrant detectors essentially measured the tilt of the wavefront averaged over a two inch aperture. The wavefront tilt or error signal was calculated every 20 msec. This data was then used to calculate the various correlation functions, as explained in the next section. The correlation functions were then used to determine r_o and τ_o , as explained in section VI.C.

One conclusion which is obvious from the data is that Wallace Observatory is not a good site for an astrometric interferometer or any high resolution instrument whose sensitivity depends on the quality of "seeing". The data was taken over a period of several months from August 1976 to December 1976. However, the raw data was not recorded because no

high speed data recorder was available. The software which calculated the correlation functions in real time was continuously modified until late September. All of the data tabulated in Appendix II was taken during October and November.

VI.B Correlation of Angle of Arrival Fluctuations

The use of the correlation functions to determine the r_o and τ_o, is discussed in the next section. This section describes the procedure used to calculate the temporal correlation functions of angle of arrival fluctuations from the error signal.

If the star trackers were perfect, the error signals would approach zero and the correlation of the error signals would not be an accurate measure of the correlation of the angle of arrival. If the servo were turned off, the error signal would be the sum of two components, one due to turbulence and one due to earth rotation. In theory, it should be possible to subtract the effect of earth rotation but in practice, the star would quickly drift out of the linear region of the quadrant error sensors.

However, the star trackers were only designed to track earth rotation. Since the response time of the servo was approximately 4 sec, the correlation functions of the error signal should be a reasonable approximation of the correlation functions of the wavefront for lags less than 4 seconds.

In addition, the 4 sec response time of the trackers, as explained in chap 5, result in a constant servo error of 2 arc sec.

This is the angular motion of Polaris in 4 sec of time. While this offset would not affect opération of the interferometer, since both star trackers would have the same offset, it does have an effect on the calculation of the correlation functions. The relation between the error signal and the angle of arrival fluctuations is illustrated in eq. VI.1 to VI.4.

$$Error(t) = Atmosphere(t) + Servo\ offset \qquad VI.1$$

$$\langle Error \rangle = \langle Offset \rangle \qquad VI.2$$

$$R_{ERR}(\tau) = \langle Err(t)\, Err(t+\tau) \rangle \qquad VI.3$$

$$R_{ERR} = R_{Atm} + (Offset)^2 \qquad VI.4$$

With eq. VI.4 it is possible to calculate the correlation fucntions of the wavefront tilts using the error signal from the star trackers. However, another source of error must also be considered. Eq. VI.2 becomes eq. VI.5 when photon noise is added.

$$Err(t) = Atm(t) + offset(t) + e(t) \qquad VI.5$$

e(t) is the error due to photon noise

Since the error signal E(t) is calculated from the number of photons detected in the 4 phototubes using eq. V.I and V.2, the statistics of e(t) are easily calculted to be eq. VI.7 (see App.

I).

$$\langle (\Delta N_i)(\Delta N_j) \rangle = N_i \delta_{ij} \qquad \text{VI.6}$$

$$\sigma_e^2 = \langle e(t)\, e(t) \rangle = \frac{1}{\sum_{i=1}^{4} N_i} \qquad \text{VI.7}$$

N_i is the number of photons detected for each measurement interval (20 msec) in the i'th phototube

The effect of photon noise is to produce a spurious increase in the autocorrelation functions at zero lag. Eq. VI.4 should be changed to eq. VI.8 when calculating autocorrelations.

$$R_E(\tau) = R_{Atm}(\tau) + Offset^2 + \sigma_e^2\, \delta(\tau) \qquad \text{VI.8}$$

VI.C Estimate of r_o and τ_o from Wavefront Tilt Correlations

From chap. 2 it is possible to derive the shape of the autocorrelation function for Kolmogorov turbulence. The shape of this autocorrelation function is characterized by two parameters, from which it is possible to calculate r_o and τ_o.

The spatial autocorrelation of the fluctuations of angle of arrival from eq. II.29 is

$$D_\alpha(r) \propto r^{-1/3} \qquad \text{II.29}$$

If we assume Tayler's hypothesis, $r=v\tau$, where v is the transverse wind speed, the temporal autocorrelation of the wavefront tilt is simply eq. VI.9.

$$R_\alpha(\tau) \propto \tau^{-1/3} \qquad \text{VI.9}$$

Eq. II.29 is not valid for $r<l_o$, the inner scale of turbulence. For $r<l_o$ the correlation is a constant approximately equal to $D_\alpha(l_o)$. The temporal correlation of the wavefront tilt should therefore exhibit the same behavior. However, the star trackers average the wavefront tilt over a 1.75 inch aperture, much larger than the inner scale of turbulence, hence $R_\alpha(\tau)$ should level off at $\tau = 1.75\text{inch}/v$ instead of l_o/v. Fig VI.1 is an example of the data taken at Wallace Observatory compared with the Kolmogorov spectrum. The seeing was quite good for Wallace Observatory when the data was taken for figure VI.1.

It can be seen in fig VI.1 that the Kolmogorov spectrum is a good fit to the wavefront tilt data. The value of $R_\alpha(0)$ is inversly proportional to r_o as derived in chapter 2 eq. II.24.

$$r_o = \frac{9.2\,\lambda}{\left[R_\alpha(0)\right]^{1/2}} \qquad \text{II.24}$$

r_o in cm

Data 3:34 10/29/76

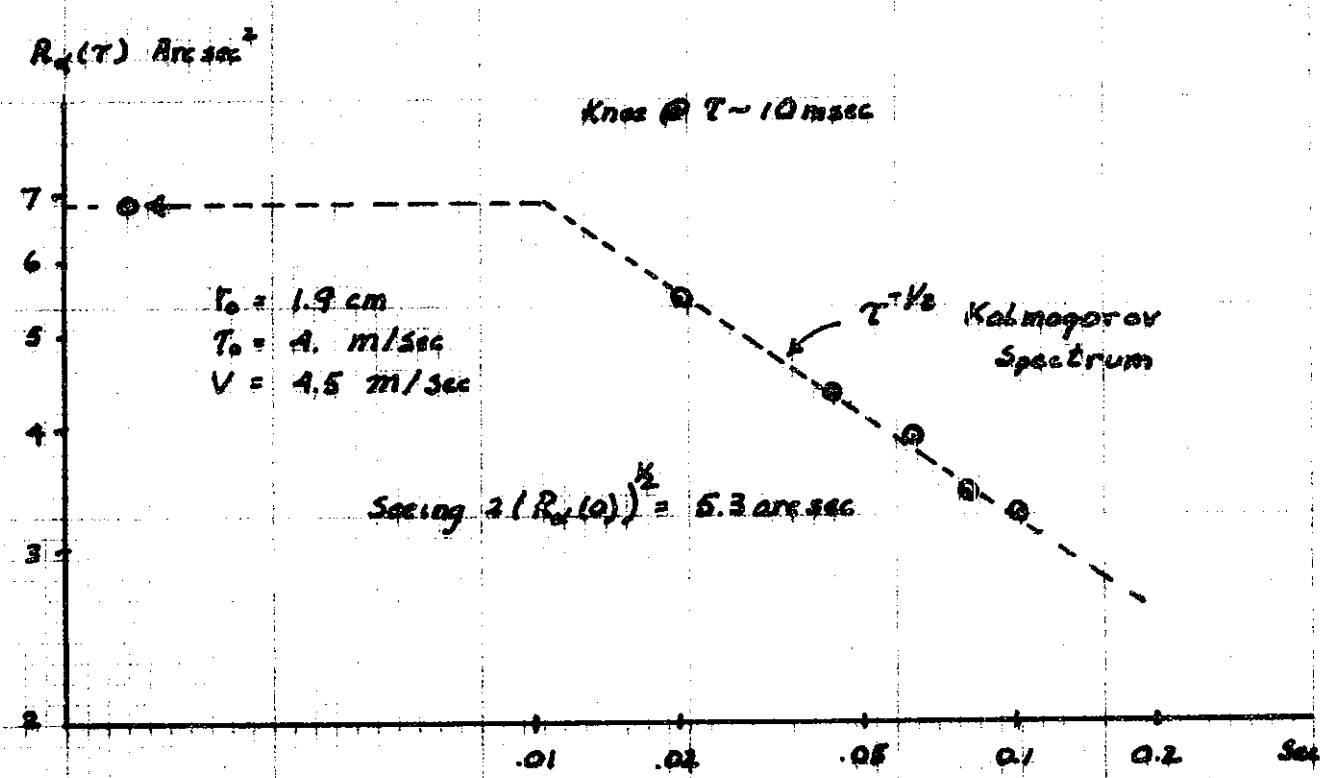

Fig. VI.1 Log R_α vs Log τ

λ in microns

R_α in arc sec^2

The wind speed can be determined by the position of the knee and the 1.75 inch aperture of the star tracker using eq. VI.10. The quantity τ_o then can be calculated using eq. VI.11.

$$V = 1.75 / \tau_{knee} \quad \text{effective wind speed} \qquad \text{VI.10}$$

$$\tau_o = \frac{r_o}{V} \qquad \text{VI.11}$$

Figure VI.1 shows that the data within a limited range is in excellent agreement with a Kolmogorov spectrum and Tayler's hypothesis. However for long lags (large τ), three effects make interpretation of the data difficult. The first is that the Kolmogorov spectrum is valid only to the outer scale of turbulence. In addition Tayler's hypothesis would not be valid for large τ because over a long period of time, several seconds, the turbulence cannot be considered frozen. Last of all, for long lags the time constant of the star tracker servoes would invalidate the assumption that the error signal is a good approximation of the wavefront tilt.

However, the region of the autocorrelation function of greatest interest for interferometry is the region where the measurements are known to be valid and where the measurements agree with theory.

VII Astrophysical Applications of Astrometry

VII.A Introduction

This chapter explains the motivation for the thesis. The present lack of excitement in optical astrometry is due in part to the extreme length of time necessary to collect data. In addition, the state of the art in astrometry instrumentation has not advanced at the same rate as other areas of astronomy. However, the development of a new instrument such as the astrometric interferometer will take a great deal of effort which cannot be justified if the only goal is "another decimal point". The increased accuracy must have astronomical or astrophysical significance.

Sometimes a new instrument is proposed because "it has never been done before" and "who knows what we'll find". While both of these arguements are valid for the astrometric interferometer, there are a number of current astronomical problems which could be resolved with an astrometric interferometer.

Traditional application of astrometry would be profoundly affected if accuracy were increased by two orders of magnitude . Proper motion surveys which would have taken 200 years could now be completed in 2 years. Since the history of photographic astrometry is slightly less than 100 years old, most of the historical data could be verified in the first year of

operation.

The rest of this chapter describes three possible applications of an astrometric interferometer, gravitational deflection of light, search for planets, and measurement of absolute parallax. The measurement techniques used for these applications, are in most cases, minor variations of current techniques. The exception is the measurement of parallax. A variation of this technique might one day be used to measure distances to objects, such as quasars, for which there are no background stars or objects (VII.D).

VII.B. Gravitational Deflection of Light

The gravitational bending of light is one of the classic tests of general relativity. The deflection of light due to the gravitational field of the sun has been calculated to be [67]

$$\Delta\alpha = 0.0041 \left(\frac{1+\cos\alpha}{1-\cos\alpha}\right)^{\frac{1}{2}} \text{arc sec} \qquad \text{VII.1}$$

where α is the angle between the star and the center of sun. For a star at the limb of the sun $\alpha = 0.27$ degrees and $\Delta\alpha = 1.75$ arc sec

The first experimental test came in 1919 during an eclipse of the sun. Until 1968 all gravitational deflection experiments were conducted during eclipses. The accuracy of

these measurements were roughly 10% or 0.2 arc sec. The portable telescopes used for eclipse observations are obviously inferior to permanent astrometric observatories. In addition the short duration of an eclipse makes it impossible to improve accuracy by taking thousands of plates and averaging the results.

The most accurate deflection measurements at present are radio VLBI measurements, slightly more than an order of magnitude more accurate than optical measurements. For an optical astrometric interferometer with 0.0001 arc sec accuracy a confirmation of eq. 2.3 to 1% is possible without daytime operation (α=45 deg). Confirmation to 0.1 % would require the measurement of stellar positions within α=4.5 degrees of the sun. Confirmation to 0.01 % would be possible only if the interferometer were built at the site of a future eclipse.

The gravitational deflection effect is also observable during an occultation of a star by a planet. The effect is greater than 10^{-4} arc sec for the planets Venus, Mars, Jupiter, Saturn, Uranus, and Neptune. For Jupiter, the gravitational effect would be significant ($> 10^{-4}$) as far as 50 arc min from the planet. At the limb of Jupiter, the effect is approximately 0.07 arc sec. While this implies that a measurement to 0.15% accuracy is possible, in practice, the short duration of an occultation (< 1 hr) would probably limit accuracies to 0.3%, about a factor of 3 more accurate than night time solar deflection measurements and a factor of 3 less

accurate than daytime solar deflection measurements.

The gravitational deflection of starlight due to the earth can be calculated from a formula very similar to eq.2.3 except the constant 0.0041 arc sec would be replaced by 2.8×10^{-4} arc sec. For a ground based observatory looking at a star 45 degrees from zenith the effect is 1.1×10^{-4} arc sec. For differential measurements over a 10 deg field of view the effect of the earth's gravitational field is less than 3.0×10^{-5} arc sec.

The gravitational deflection experiment, as a test of general relativity measures the PPN (parameterized post newtonian formalism) parameter γ . Another experiment that measures this parameter is a light or radio transit time measurement which measures the time delay caused by the gravitational field. Since light deflection can be viewed as a differential time delay, we would expect that the time delay experiment would ultimately be more sensitive. The time delay experiment is carried out with radar astronomy or with space probes. The high degree of agreement of this and other first order tests of general relativity has led most astrophysicists to consider only those theories that agree with general relativity at low gravitational field strengths. While the measurement of the gravitational deflection of light will be an important application of the astrometric interferometer, the effect will soon be treated as a source of systematic error to be eliminated in a search for other effects.

VII.C Search for Planets and Dark Objects

VII.C.1 Historical Introduction

The detection of dark or faint companions of stars dates back to 1844 when Bessel anounced the presence of a perturbation in the proper motion of Sirius. The companion of Sirius, a white dwarf was seen visually in 1862. In 1846 the planet Neptune was found from the perturbation it produced in the orbit of Uranus. The search for dark objects has historically been one of the most fruitful applications of astrometry.

Two methods are currently used to detect dark objects. Both techniques detect the presence of an unseen object by its gravitational influence of a nearby visible star. One method is astrometric detection where the orbit of the visible star around the system's center of mass produces a periodic change in the star's position. The second method is spectroscopic detection which measures the periodic doppler shift due to the orbital motion of the visible star.

There are over 800 spectroscopic binaries [10]. The mass of the unseen companion, when known indicate that these are multiple star systems. There are 17 unresolved astrometric binaries [58] with large and undisputed astrometric motions >0.04 arc sec. The calculated mass of the companions indicate

in all 17 cases that the companion is a star. There are 15 stars that show significant astrometric perturbations, which are suspected to be due to an unseen companion [58]. At one time it was claimed that several of these stars had planets. In addition to the 15, Van de Kamp has claimed and defended the existance of two planets around Barnard's star.

A short summary of the recent arguments for and against the existance of planets is given for the interested reader. Van de Kamp first reported the presence of a single planet around Barnard's Star (1963) [68]. Subsequently, he reported the presence of two planets (1969)[69] using the huge quantity. of historical data taken at Sproul Observatory. Gatewood et. al. then published an unsuccessful search for planets around Barnard's Star in 1973[63] using data from Allegeny and Van Vleck observatory. Van de Kamp subsequently reanalysed his data. This involved remeasuring the plates and was not purely a numerical exercise.

The new results[64] still showed the presence of two planets but their total astrometric perturbation was smaller by aproximately a factor of two. Van de Kamp's data was independently analysed by Jensen et. al. [70] who reported the probable existance of three planets. The analysis however, was carried out not with the raw data but with the residuals calculated by Van de Kamp. Sproul, Van Vleck, and Allegany observatories have actively searched for dark objects around nearby stars since the late 1930's.

There is no consensus. The proper motion of Barnard's star is 10. arc sec/year the largest of any star. This alone made it one of the most heavily studied objects for astrometers. Much more astrometric data is available for Barnard's star than any other star. On the other hand it is not clear that all systematic errors have been deleted and hence the larger quantity of data may or may not result in higher accuracy. The reported perturbations of Barnard's star is 0.009 arc sec for the larger planet (10^{-3} $M_{\odot}$, 26 year). The smallest perturbation of the 17 undisputed and unresolved astrometric double stars is 0.04 arc sec. Also, the reported perturbations of Barnard's Star 0.009 arc sec is significantly smaller than the average error (0.016 arc sec) in the general catalog of parallaxes [71]. It is my admittedly biased opinion that the question of the existance of planets around Barnard's or any other star will not be resolved until the next generation of astrometric instruments are built.

VII.C.2 Instrumental Limitations for the Detection of Planets

For a planetary system with one large planet, the astrometric perturbations are expressed by eq. VII.2. Eq. VII.3 gives the size of the spectroscopic perturbations.

$$\Delta\Theta = \frac{R\ m}{L\ M} \text{ arc sec} \qquad \begin{array}{l}\text{where m, M are in M}\\ \text{L in parsec}\\ \text{R in A.U.}\end{array} \qquad \text{(VII.2)}$$

$$\frac{\Delta V}{C} = m \frac{1}{M\ R} * 10^{-4} \quad \text{spectroscopic motion} \qquad \text{(VII.3)}$$

The sensitivity of current spectroscopic techniques is approximately 0.7 km/sec [72]. At 5000 Å this corresponds to 0.011 Å shift in the center of a spectral line. Although 0.011 Å is considerably smaller than the width of stellar spectral lines, this level of accuracy is not sufficient to detect planets. For example a Sun-Jupiter system would produce a spectroscopic perturbation of 26 m/sec. Barnard's star would produce a shift of 44 m/sec.

In order to detect a Sun Jupiter system with spectroscopic techniques, a number of systematic errors must be eliminated. The doppler shift caused by the Earth's motion around the Sun is 30 km/sec, the shift caused by the moon's motion is 10 meters/sec. However, the most serious errors are in the wavelength calibration of the spectrometers. For most dispersive spectmeters, those using gratings or prisms, the wavelengths are calibrated with a lamp which emits a large number of lines. For detection of planets, it will be neccessary to use a spectrometer which directly compares the stellar line with a laser wavelength standard. There are two types of spectrometers which are suitable for detection of planets, fourier spectrometers and heterodyne spectrometers. These spectrometers unfortunately are much less sensitive than dispersive spectrometers, which can monitor many spectral lines simultaneously.

The photon noise limit for spectroscopic detection of planets may be estimated as follows. Assume a thermally broadened line (6000 K) of 10km/sec width (0.16 A) is monitored with a spectrometer. Also assume that the desired accuracy is 1 meter/sec (signal/noise of 20 for Sun-Jupiter). This would require the spectrometer to detect 100 million photons in the spectral line. Using a 10% quantum efficiency detector on a 5 meter telescope, the integration time for a 10.0 mag star is approximately 100 hours.

The spectroscopic detection of planets may be possible if an instruement with very high wavelength accuracy is built. However, the search for planets would be limited to bright stars and would require a great deal of observing time on the largest telescopes.

The accuracy of current astrometric instruments and the astrometric interferometer has been discussed. Table VII.1 lists the spectroscopic and astrometric perturbations of three planetary systems. The detection of Sun-Earth systems would not be possible with the next generation of astrometric or spectroscopic instruments.

Table VII.1

	Astrometric	Spectroscopic
Barnard's Star	0.009 arc sec	44 m/sec
Sun-Jupiter (10 pc)	0.001 arc sec	26 m/sec
Sun-Earth (10 pc)	$0.6*10^{-6}$ arc sec	0.2 m/sec

VII.C.3 Theoretical Constraints on the Formation of Planets

In current theories, the formation of planets is intimately related to the formation of stars. All the physical processes that inhibit the formation of stars will also inhibit the formation of planets. In addition, tidal forces and the heat generated by the protostar will inhibit the process of planet formation near the star.

In most cases, the astrometric detection of a single planet will have very little effect on current theories of star and planet formation. The reason is that either the theory has not been worked out in sufficient detail to predict the size and/or orbit of planets, or the theories have so many free parameters that any number of planets including zero may orbit about a given star. However, a search for planets will provide important statistical information on the existance and angular momentum of planets which may enable more detailed theories to be formulated.

VII.D The Measurement of Parallax Without Background Stars

In photographic parallax measurements, the distance to a target star is determined by measuring the position of the target star relative to a number of background stars. The astrometric interferometer, because of its higher accuracy of

10^{-4} to 10^{-5} arc sec, needs background stars that are 10 to 100 kiloparsec away from the sun. If the star is brighter than the magnitude limit of a ground based interferometer, aprox. 10 mag. , its luminosity or absolute magnitude would have to be extremely high, from -5 to -10 mag even when interstellar absorption is ignored. A crude estimate for absorption by interstellar dust of 0.8 mag/kiloparsec [10] means that a background star at 10 kiloparsec would have to have a luminosity of -13 mag, 10^7 solar luminosity, if its apparant magnitude is to be +10 mag. No stars this luminous are known to exist. As a comparison, novae have a peak luminosity of aproximately -8 mag and supernovae, -17 to -19 mag.

VII.D.1 General Method

The first method derives the distance to two stars from the measurements of the angle between these two stars as a function of time. The major difference between this method, to be described, and photographic data analysis is that in photographic techniques, the parallax motion of the star is described by some astrometers in a tangent plane coordinate system [61] while I will describe its motion in spherical coordinates. The tangent plane coordinate system is of course an approximation to the exact formulation. This approximation deletes a second order effect which is the basis of measuring parallax without reference stars. The fact that the effect is a

second order effect results in the loss of accuracy of a factor 5 to 10.

This method is best illustrated in fig VII.1. Two stars are located 90 degrees apart on the ecliptic. By measuring the angle between the two stars four times in one year when the earth is at postions a,b,c, and d it is possible to determine the distance to both stars. The measurements at a and c differ by exactly the parallax of star A since the parallax for star B for these two measurement points is zero. Similarly, measurements at positions b and d will give the absolute parallax for star B. More generally, the angle between two stars will change in a sinusoidal fashion as a function of time eq. VII.4. This change is due to the fact that both stars are at a finite distance from the sun. This sine wave with a period of one year is characterized by two parameters, amplitude and phase (eq. VII.4). These two parameters are determined by the position of the two stars eq. VII.5 and VII.6.

$$\text{Angle between stars} = A \sin(\omega_0 t + \phi) \qquad \text{VII.4}$$

$$A = f(\alpha_1, \delta_1, r_1, \alpha_2, \delta_2, r_2) \qquad \text{VII.5}$$

$$\phi = g(\quad " \quad) \qquad \text{VII.6}$$

$$\omega_0 = 2\pi/\text{year}$$

If we previously measure the values of α_1, δ_1, α_2, δ_2 and measure A and ϕ eq. VII.5 and VII.6 become two equations in two unknowns. The solution of these equations yields the

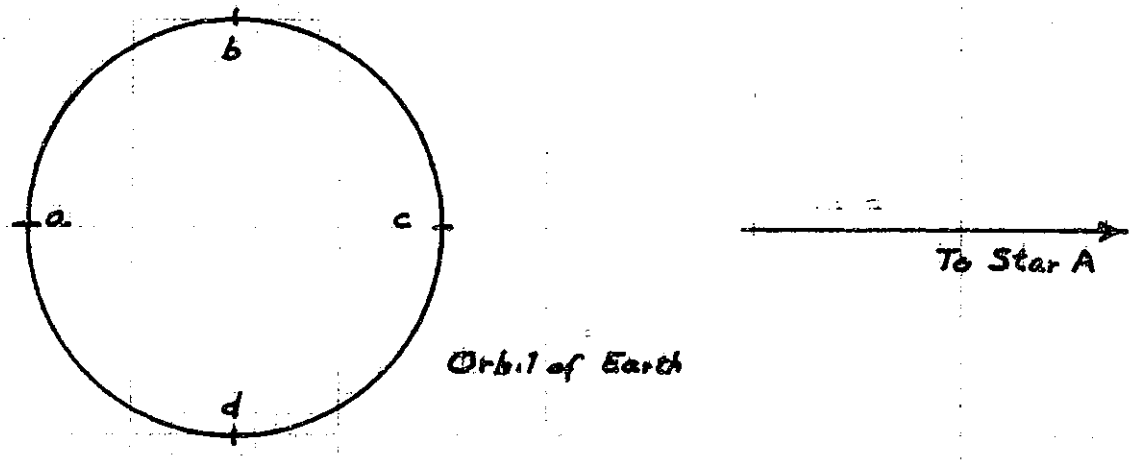

Measurement of Absolute Parallax

Fig. III. 1

Measurement of angle between A & B at points a, and c give absolute parallax of star B.

distances r1 and r2. (α_1, δ_1, and r1 are the spherical coordinates of star 1)

In the following calculations, we may assume that the two stars have the coordinates

$$\alpha_1 = 0 \qquad \alpha_2 = \alpha_2$$
$$\delta_1 = \delta_1 \qquad \delta_2 = \delta_2$$
$$r_1 = r_1 \qquad r_2 = r_2$$

The position of the earth as a function of time is then

$$\alpha_E = \omega_0 t \qquad \delta_E = 0 \qquad r_E = 1\ A.U.$$

A circular orbit is assumed to simplify the algebra.

The angle between the stars as seen from the earth as a function of time is then described by eq. VII.7.

$$\cos(\theta(t)) = \frac{(\vec{S}_1 - \vec{E}) \cdot (\vec{S}_2 - \vec{E})}{|\vec{S}_1 - \vec{E}\ |\ |\vec{S}_2 - \vec{E}\ |} \qquad \text{VII.7}$$

However, since r1 and r2 are so large compared to 1 A.U., the equation may be simplified by dropping the second and higher terms. For stars at a distance of 5 parsec or more, the second order term will be 10^{-12} radians or 2×10^{7} arc sec. $\theta(t)$ may be expressed as eq. VII.8.

$$\Theta(t) = \Theta_0 + \Delta\Theta(t) = \Theta_0 + \pi_0 \sin(\omega_0 t + \phi) \qquad \text{VII.8}$$

The right side of eq. VII.7 is simplified to eq. VII.9.

$$\cos(\Theta(t)) = \cos\Theta_0 - \sin\Theta_0 \, \Delta\Theta(t) \qquad \text{VII.9}$$

Further simplifying and solving for $\Delta\Theta(t)$ we get eq. VII.10.

$$\Delta\Theta = A\cos\omega_0 t + B \sin\omega_0 t \qquad \text{VII.10}$$

where

$$A = \frac{1}{r_1}(\cos\delta_2\cos\alpha_2 - \cos\Theta_0\cos\delta_1)/\sin\Theta_0 + \frac{1}{r_2}(\cos\delta_1 - \cos\Theta_0\cos\delta_1\cos\alpha_2)/\sin\Theta_0 \qquad \text{VII.11}$$

$$B = \frac{\left[\frac{1}{r_1}(\cos\delta_2\sin\alpha_1) - \frac{1}{r_2}(\cos\Theta_0\cos\delta_2\sin\alpha_2')\right]}{\sin\Theta_0} \qquad \text{VII.12}$$

Four measurements of $\Delta\Theta(t)$ at times such that $\omega_0 t = 0$, $\pi/2$, π, and $3\pi/2$ would enable us to calculate A and B from eq. VII.10. If the measurement error for each measurement of Θ

were σ_θ, the probable error for the parameters A and B would be $\sigma_\theta/\sqrt{2}$. Since A and B can be derived from measurement, eq. VII.11 and VII.12 represent the two equations for two unknowns r1 and r2.

$$\text{Absolute parallax} = \pi_i = 1/r_i$$

$$\pi_1 = \frac{A(\cos\Theta_0 \sin\alpha_2 \cos\alpha_2) - B(\cos\delta_2 - \cos\Theta_0 \cos\delta_2 \cos\alpha_2)}{-\sin\Theta_0 \cos\delta_1 \cos\delta_2 \sin\alpha_2} \quad \text{VII.13}$$

$$\pi_2 = \frac{A\cos\delta_2 \sin\alpha_2 - B(\cos\delta_1 \cos\alpha_2 - \cos\Theta_0 \cos\delta_1)}{-\sin\Theta_0 \cos\delta_1 \cos\delta_2 \sin\alpha_2} \quad \text{VII.14}$$

In order to calculate the probable error in the determination of π_1 and π_2 we may use eq. VII.15.

$$\sigma_\pi = \frac{\sigma_\theta}{\sqrt{2}} \left[\left(\frac{\partial\pi}{\partial A}\right)^2 + \left(\frac{\partial\pi}{\partial B}\right)^2 \right]^{1/2} \quad \text{VII.15}$$

The quantity in the square brackets in eq. VII.15 represents the loss in accuracy when this technique is used. For the special case $\delta_1 = \delta_2$ the factor is expressed in equation VII.16.

$$\left[\qquad\right]^{1/2} = \frac{\left[1+\cos^2\Theta_0 - 2\cos\Theta_0\cos\alpha_2\right]^{1/2}}{\sin\Theta_0\cos\delta\sin\alpha_2} \qquad \text{VII.16}$$

In particular, we see that for $\delta_1 = \delta_2 = 0$ the factor is $1/\sin(\Theta_0)$. If the field of view of the astrometric interferometer is 10 degrees, the error in absolute parallax would be 5.8 times the error of the relative measurement.

The analysis that led to eq.VII.16 assumed that the positions of the stars in ecliptic coordinates are known. Errors in the values used for α and δ of the stars will result in an error in the parallax. Fortunately the required accuracy for the absolute coordinates is not very great. Eq. VII.17 states the level of accuracy required.

$$\left(\frac{\partial\pi}{\partial A}\right)^2 + \left(\frac{\partial\pi}{\partial B}\right)^2 > \left(\frac{\partial\pi}{\partial\alpha_1}\right)^2 + \cdots \left(\frac{\partial\pi}{\partial\delta_2}\right)^2 \qquad \text{VII.17}$$

An examination of VII.13 and VII.14 shows that this would be approximately satisfied if eq. VII.18 is satisfied.

$$\frac{\sigma_A}{A} > \sigma_\alpha, \sigma_\delta, \text{etc.} \qquad \text{VII.18}$$

The sqrt(A**2+B**2) ,the relative parallax, must be less than one arc sec and we may assume $\sigma_A = 10^{-4}$ arc sec. Therefore must be less than 10^{-4} radians. For a 10 meter astrometric interferometer, the measurement of absolute parallax requires that the absolute coordinates of the stars be known to an accuracy of 20. arc sec. In addition eq. VII.14 and VII.15 the absolute coordinates are needed to correct for the effects of differential stellar abberation. For 10^{-4} arc sec accuracy, the absolute positions of the stars must be known to 6 arc sec.

VII.D.2 Absolute Parallax of Spectroscopic Binaries

The second method uses both astrometric measurements and spectroscopic measurements to determine the distance to a star. In principle the technique works as follows. From spectroscopy of a double star, the velocity of the star as a function of time can be measured. The integral of the velocity is the distance. Astrometry measures the angular motion of the star; since the angular motion is simply the motion of the star divided by the distance to the star these two measurements can

be used to determine the distance to the star.

Astrometric observations of course measure transverse motion, and doppler measurements measure radial motion. The motion of two objects in a stable orbit about their center of mass is characterized by seven parameters. Measurement of the motion of one of the two binaries through a full cycle is sufficient to determine all the parameters.

In photographic astrometry, the opportunity to combine spectroscopic and astrometric data is rare. As explained in the section describing the search for planets, astrometry and spectroscopy are complementary techniques. The objects for which spectroscopy will yield results are close binary systems where orbital velocities are high. Astrometry is sensitive to binary systems that have widely separated components. The increase of accuracy possible with the astrometric interferometer should create a sizeable area of overlap. A similar technique is currently being used with speckle interferometry.

As mentioned previously, this technique is accurate only for double star systems that are detectable both astrometrically and spectroscopically. Systems with short orbital periods (weeks) usually will not have a measureable astrometric motion, while those with very long periods (> 10 years) usually will not have a measurable spectroscopic motion. For an ideal system with a period of aproximately 3 years and a peak to peak astrometric motion of 5 A.U., absolute parallax

measurements to $2.x10^{-5}$ arc sec (1σ) accuracy are possible with 10^{-4} arc sec astrometric accuracy.

VIII Conclusions

Currently, there are no operational astrometric interferometers. This thesis described a prototype of an astrometric interferometer and three problems associated with the operation of such an instrument. The first and most important problem is the isoplanatic patch problem. The small size of the isoplanatic patch, a few arc sec for high resolution instruments, would render other high resolution instruments usless for astrometry of widely separated stars. The solution of the isoplanatic patch problem provided the initial motivation for the thesis.

The second problem is one of a number of problems which illustrates the fact that new measurement techniques are necessary to take advantage of a radically new instrument. The problem was the measurement of absolute parallax. Current techniques measure the distance to stars by measuring changes in the apparant position of stars relative to background stars. As explained in the last chapter, for practical purposes, there are no background stars. While I had recognized the existance of the problem, much of the motivation for finding a specific solution came from the reviews of an NSF proposal for an interferometer.

Two important atmospheric parameters r_o and τ_o determine the sensitivity of all high resolution instruments. r_o is the maximum usable aperture for a Michelson interferometer and

τ_0 is the time during which the atmosphere can be considered frozen. In the early days of speckle interferometery, τ_0 was determined by a trial and error process. In the next version of the astrometric interferometer, these parameters calculated in real time will be used to optimize the operation of the fringe tracking servo under changing atmospheric conditions.

Several conclusions may be drawn. One is that the most important problem, isoplanatism, has a solution at least in theory. Another that the Kolmogorov spectrum provides an excellent description of atmospheric turbulence for astronomical applications. Last of all, it is obvious that this thesis is only the first step toward an operational astrometric interferometer.

The second step will start immediately after the first step and will be funded by a small NSF grant. Hopefully, the third step, the construction of an operational instrument will be possible in the not too distant future. In my opinion, the results will be worth the considerable effort needed to develope the instrument.

Appendix I Error Estimation

The measurement of any quantity involves noise. By analysing the results of a number of independent measurements, it is possible to derive an estimate of the quantity being measured as well as the probable error of a single measurement. While the measurement of the probable error is simple, it is often desirable to estimate the probable error before the instrument is built.

For the astrometric interferometer, the predominent source of noise is hopefully, photon noise. Photon noise has the property that the mean is equal to the variance. With this information, it is possible to estimate the probable error in fringe phase or visibility due to photon noise.

For example, the phase, ϕ = arctan ((a-c)/(b-d)) is a function of four random variables that obey possion statistics. The probable error σ_ϕ may be calculated using the following technique.

If we let the quantity that is being measured be a function f of n independent random variables $x_1, \ldots x_n$, then we express the mean and variance of f by way of a taylor series expansion.

$$f = f(\bar{x}_1, \cdots, \bar{x}_n) + \sum_i \Delta x_i \frac{\partial f}{\partial x_i} + \sum_{i,j} \frac{\Delta x_i \Delta x_j}{2} \frac{\partial^2 f}{\partial x_i \partial x_j}$$

$$+ \cdots \text{ higher order terms}$$

$\langle\ \rangle$ denotes ensemble average

$$\langle f \rangle = f(\bar{x}_1 \cdots \bar{x}_n) + \sum_i \frac{\langle \Delta x_i^2 \rangle}{2} \frac{\partial^2 f}{\partial x_i^2} + \cdots$$

where $\Delta x_i = x_i - \bar{x}_i$

and the first order term are 0

$$\left\langle \sum_i \Delta x_i \frac{df}{\partial x_i} \right\rangle = 0$$

because $\langle (x_i - \bar{x}_i) \rangle = \langle x_i \rangle - \bar{x}_i = 0$

since x's are independent random variables,

$\langle (x_i - \bar{x}_i)(x_j - \bar{x}_j) \rangle = 0$ when $i \neq j$

by definition the variance is $\langle (f - \bar{f})^2 \rangle$, so

$$\sigma_f^2 = \sum_i \langle \Delta x_i^2 \rangle \left(\frac{df}{dx_i} \right)^2 + \text{higher order terms}$$

In the trivial case of $f(x_1, \ldots, x_n) = x_1 + \ldots + x_n$ all the second order and higher derivatives are 0 and the first derivatives are 1. so

$$\langle f \rangle = \bar{x}_1 + \cdots \bar{x}_n$$

$$\sigma_f^2 = \sum_i \langle \Delta x_i^2 \rangle$$

Appendix II

This appendix lists the data from several nights of observation at Wallace Observatory. The numbers are in units of (arc sec). The tables of numbers start with the correlation function at zero lag. Each subsequent number is the function at 20, 40, 80, etc. msec lags. The lag step sizes in msec is listed along with the type of function, auto correlation, cross correlation etc.

Oct. 29 1976

time 3:33:50 sidt west az auto corr. 20msec

11.1 5.5 4.4 4.0 3.6 3.4 3.2

2.9 2.9 2.4 2.6 2.7

time 3:49:11 sidt west az auto corr. 20msec

11.3 5.3 4.0 3.6 3.3 3.4 2.9

2.7 2.5 2.4 2.6 2.4

time 3:51:15 sidt west az auto corr. 20msec

13.0 6.9 5.4 5.1 4.6 4.1 3.8

3.4 3.2 2.9 2.7 3.3

time 4:45:10 sidt west az auto corr. 80msec

6.5 3.7 2.8 2.5 2.0 1.5 1.2

1.1 1.0 1.2 1.2 1.2 1.1 1.0

1.0 .7 .5 .5 .4

time 4:47:15 sidt west az auto corr. 80msec

6.0 3.2 2.4 2.0 1.6 1.6 1.1

1.0 .9 .8 .9 .9 .7 .7

.3 .5 .3 .2 .1

Nov 12 1976

time 4:54:0 sidt az-az cross corr. 40 msec

-0.13 0.06 0 -0.09 0 0 0.15

0.2 0.05 0 -0.14 -0.04 -0.09 0

-0.04 -0.19 -0.09 -0.09 -0.14 -0.14 0.05

time 5:08:0 sidt west az-el cross corr. 40 msec

2.62 .96 .74 .52 .49 .62 .54

.49 .62 .54 .45 .36 .34

time 5:22:0 sidt west az - east el cross corr. 40msec

-.24 -0.32 -0.13 -0.13 -0.1 -0.12 -0.1

-0.02 -0.10

Nov 13 1976

time 8:40:0 sidt west az auto corr. 40msec

9.1 4.6 3.8 3.4 2.9 2.8 2.5

2.2 2.4 2.3 2.2 2.2 2.1 2.1

1.9 1.8 1.8 1.9 1.9 1.8 1.6

1.6 1.5

time 8:45:0 sidt west az auto corr. 20msec

12.7 5.6 4.6 4.2 3.6 3.5 3.3

3.1 3.2 2.9 2.8 2.7

time 10:18:0 sidt west el auto corr. 20msec

16. 7.5 6.1 5.6 5.0 4.9 4.6

4.6 4.2 3.8 3.7 3.6

Appendix III

This appendix describes the expected distributions of FASN due to photon noise. These calculations of FASN used the full wavelength modulation pattern described in chapter IV. The distributions were calculated using a monte-carlo technique. The programming was done by R. Concia. While these figures are not directly comparable with the one inch prototype, they indicate that servo operation at low light levels is possible when fringe visibility is near unity.

The graphs on the following pages represent the FASN distributions for 200 photons/sample.

Bibliography

1 Vasilevskis, Annual revies of Astronomy and Astrophysics, vol 4, p. 57, (1966).

2 Fizeau,C., Acad. Sci. Paris, Vol 66, p.934, (1868).

3 Michelson,A.,and Pease, F., Ap. J., vol 53, p.249, (1921).

4 Kababian,P., and Staelin,D., Optical Interferometer for Satellite Survalence, AFAL TR 73 447 (1974).

5 Woods Hole Summer Study on Synthetic Aperture Optics, AD 680 797 Aug. 1967.

6 Geazri,D., Labeyrie,A., and Stachnik,R., Ap. J., vol 173, L1, (1972).

7 Shao,M., and Staelin,D., J.O.S.A., vol 67, p. 81, (1977).

8 Chandrashakar,C., M.N.R.A.S., vol 112, p. 475, (1952).

9 Lawrence,R. and Strobehn,J., Proc. I.E.E.E., vol 58,p. 1523, (1970).

10 Allen,C., Astrophysical Quantities 3rd ed. (1973).

11 Kolmogorov, A., in Turbulence, Classic Papers on Statictical Theory, S.Friedlander and L.Topper, Eds. N.Y.:Interscience, p. 151, (1961).

12 Obukhov,A., Izv. Akad. Nauk. SSSR, Ser. Geogra. Geofiz., vol 13, p.58, (1949).

13 Tartarski,V. Wave Propagation in a Turbulent Medium, N.Y.:McGraw Hill, (1961).

14 Barletti,R. et. al., J.O.S.A., vol 66, p. 1380, (1976).

15 Saleh,A., IEEE J. Quantum Elec., vol QE3, p. 540, (1967).

16 Kon,A., and Feizulin,V. Radiophys Quantum Elec., vol 13, p. 51, (1970).

17 Strobehn,J., Proc. I.E.E.E., vol 56, p. 1309, (1968).

18 Gracheva,M., Izv. Vyssh. Ucheb. Zaved. Radiofiz., vol 10, p. 775, (1967).

19 Mevers,G. et. al., J.O.S.A., vol 59, p. 491, (1969).

20 Ochs,G. and Lawrence,R., J.O.S.A., vol 59, p. 226, (1969).

21 Fitzmaurice,M., et. al., J.O.S.A., vol 59, p. 7, (1969).

22 Gurvich,A., et. al.,Radiofizike, vol 11, p. 1360, (1969).

23 Ochs,G., et. al., J.O.S.A., vol 41, p. 689, (1951).

24 Mikesell, A., et. al., J.O.S.A., vol 41, p. 689, (1951).

25 Young,A., Appl. Optics, vol 8, p.869, (1969).

26 Ryznar,E., Appl Optics, vol 4, p. 1416, (1965).

27 Yura, H., J.O.S.A., vol 64, p. 59, (1974).

28 Clifford, S., et. al., J.O.S.A., vol 64, p. 148, (1974).

29 Fante, R., Radio Science, vol 10, p. 77, (1975).

30 Born, G., et. al., Appl. Optics, vol 14, p. 28, (1975).

31 Fried,D., J.O.S.A., vol 55, p. 1427, (1965).

32 Fried,D., J.O.S.A., vol 56, p. 1372, (1966).

33 Bouricius,G., & Clifford,S., J.O.S.A., vol 60, p. 1484, (1970).

34 Stephan, R.Acad. Sci., Paris, vol 76, p. 1008, (1873).

35 Currie,D., et. al., Ap. J., vol 187, p. 131, (1974).

36 McCarthy,D., and Low,F., Ap. J., vol 202, L37, (1975).

37 Debrus,S., et. al., 1969 I.C.O. 8 Conference, Reading.

38 Labeyrie,A., Astron. & Astrophy., vol 6, p. 85, (1970).

39 Blazit,A., et. al., Ap. J., vol 214, p. L79, (1977).

40 Korff,D., J.O.S.A, vol 63, p. 971, (1973).

41 Roddier,F., Topical Meeting on Imaging in Astronomy, p. ThcC6-1, (1975).

42 Session C of Topiacal meeting on Imaging in Astronomy, Cambridge, (1975).

43 Babcock,H., P.A.S.P., vol 65, p. 229, (1953).

44 Topical Meeting on Imaging in Astrometry, Cambridge, 1975.

45 March Issue of J.O.S.A. 1977.

46 Brown,H.R., and Twiss,R., Proc. Roy. Soc. A., vol 248, p. 199, (1958).

47 Johnson,M., and Betz,A., Nature, vol 250, p. 128, (1974).

48 Brown,H.R., and Twiss,R., vol 178, p. 1046, (1956).

49 Johnson,M, et. al., Phy. Rev. Let., vol 33, p. 1617, (1974).

50 Wang,C., Opt. Comm., vol 14, p. 200, (1975).

51 Shapiro,J., J.O.S.A., vol 66, p. 469, (1976).

52 Korff,D, et. al., J.O.S.A., vol 65, p. 1321, (1975).

53 Schlesinger,F., Probleme der Astronomie:Seelinger Festschrift (Berlin:Springer).

54 Strand,K., Publ. U.S. Naval Obs., 20:PT.I, 9, (1971).

55 Dicke,R., and Goldenberg,M., Phy. Rev. Let., vol 18, p. 313, (1967).

56 Hill,H., and Stebbins,R., Ap. J., vol 200, p. 471, (1975).

57 Land,G., Astron. J., vol 55, p. 141, (1950).

58 Van De kamp,P., Annual Review of Astron. and Astrophy., vol 13, p. 295, (1976).

59 Oleson,J., et. al., Applied Opt., vol 13, p. 206, (1974).

60 Kolchinskii,I., in Optical Instability of the Earth's Atmosphere, Ed. N. Kucherov, (Jerusalem:Israel program for Scientific Translations).

61 Kamp,P. van de, in Astron. Techniques, Ed W. Hiltner, University of Chicago press:Chicago, (1962).

62 Upgren,A., et. al., Astron. J., vol 82, p. 227, (1977).

63 Gatewood,G., et. al., Astron. J., vol 78, p. 769, (1973).

64 Kamp,P. van de, Astron. J., vol 80, p. 658, (1975).

65 RCA data sheet on C31034A photo tube Oct. 1976.

66 Smylie,D.,Mansinha,L., Sci. Am., vol ?, p. 80, (197?).

67 Misner,C., et. al., Gravitation, San Fransico:W.Freeman, (1973).

68 Kamp,P. van de, Astron. J., vol 52, p. 226, (1963).

69 Kamp,P. van de, Astron. J., vol 74, p. 238, (1969).

70 Jenson,O., Astron. J., vol 78, p. 1104, (1973).

71 Jenkins,L., Supplement to the General Catalog of Trigonometric Stellar Parallaxes; New Haven, (1963).

72 Griffin, R., and Gunn,J., Ap. J., vol 74, p.545, (1974).